Constraints on the superconducting state of Sr_2RuO_4 from elastocaloric measurements

Grgur Palle [1,*] Clifford Hicks [2,3] Roser Valentí,[4] Zhenhai Hu [3] You-Sheng Li,[3] Andreas Rost,[5]
Michael Nicklas [3] Andrew P. Mackenzie,[3,5] and Jörg Schmalian[1,6]

[1]*Institute for Theoretical Condensed Matter Physics, Karlsruhe Institute of Technology, 76131 Karlsruhe, Germany*
[2]*School of Physics and Astronomy, University of Birmingham, Birmingham B15 2TT, United Kingdom*
[3]*Max Planck Institute for Chemical Physics of Solids, 01187 Dresden, Germany*
[4]*Institute for Theoretical Physics, Goethe University Frankfurt, 60438 Frankfurt am Main, Germany*
[5]*Scottish Universities Physics Alliance, School of Physics and Astronomy, University of St. Andrews, St. Andrews KY16 9SS, United Kingdom*
[6]*Institute for Quantum Materials and Technologies, Karlsruhe Institute of Technology, 76344 Eggenstein-Leopoldshafen, Germany*

Strontium ruthenate Sr_2RuO_4 is an unconventional superconductor whose pairing symmetry has not been fully clarified, despite more than two decades of intensive research. Recent NMR Knight shift experiments have rekindled the Sr_2RuO_4 pairing debate by giving strong evidence against all odd-parity pairing states, including chiral p-wave pairing that was for a long time the leading pairing candidate. Here, we exclude additional pairing states by analyzing recent elastocaloric measurements [Y.S. Li *et al.*, Nature **607**, 276 (2022)]. To be able to explain the elastocaloric experiment, we find that unconventional even-parity pairings must include either large $d_{x^2-y^2}$-wave or large $\{d_{xz} \mid d_{yz}\}$-wave admixtures, where the latter possibility arises because of the body-centered point group symmetry. These $\{d_{xz} \mid d_{yz}\}$-wave admixtures take the form of distinctively body-centered-periodic harmonics that have horizontal line nodes. Hence $g_{xy(x^2-y^2)}$-wave and d_{xy}-wave pairings are excluded as possible dominant even pairing states.

I. INTRODUCTION

The nature of the superconductivity of strontium ruthenate (SRO) remains elusive. In the three decades following its discovery [1], an impressive array of experiments have been performed with high precision and on exceedingly pure samples [2–6]. Yet the most straightforward interpretations of the various experimental results are regularly at odds with one another. Although many proposals [7–21] have been made on how the assortment of experimental results might be reconciled, no consensus has formed around which proposal is the correct one. Before presenting our results, in the next six paragraphs, we review what is currently known about the pairing state. This literature review is not essential to our argument and can be skipped.

The superconductivity (SC) of SRO is unconventional. This has been established early on by the absence of a Hebel-Slichter peak [22] in the NMR relaxation rate $1/T_1$ [23–25], and by the large suppression of the SC transition temperature T_c by nonmagnetic impurities [26–29] that saturates the Abrikosov-Gor'kov bound [30,31]. Subsequent experiments have only further confirmed the unconventional character of SRO's SC.

The pairing of SRO is more likely to be even than not. Recent NMR Knight shift [32–35] and polarized neutron scattering [36] experiments strongly favor singlet pairing, as do numerous studies [6,37] indicating that the in-plane critical

field $B_{c2\parallel ab}$ is Pauli limited [38]. Although the observation of π phase shifts [39] and half-quantum vortices [40–42] is at tension with even-parity SC, possible explanations do exist [10,43,44]. Reconciling an 80% drop in the in-plane Knight shift [35] with triplet pairing, or a strained critical field anisotropy $B_{c2\parallel ab}/B_{c2\parallel c} \sim 3$ [45] far below the SC anisotropy $\xi_{ab}/\xi_c \sim 60$ [46,47] without Pauli limiting [6], is significantly more challenging, but perhaps possible [48,49].

The evidence for time-reversal symmetry breaking (TRSB) is mixed. Zero-field muon spin relaxation (ZF-μSR) [50–54] and polar Kerr effect [55,56] experiments indicate TRSB at a T_{TRSB} at or very near T_c, yet the current response of micrometer-sized Josephson junctions exhibits time-reversal invariance [57,58]. Under $\langle 100 \rangle$ uniaxial pressure, ZF-μSR [53] observes a large splitting between T_{TRSB} and T_c,[1] yet no signatures of a TRSB phase transition below T_c have been found in heat capacity [59] or elastocaloric [60] measurements. Under disorder and hydrostatic pressure, no splitting between SC and TRSB is observed in ZF-μSR [54]. Preliminary ZF-μSR measurements point towards splitting of SC and TRSB under $\langle 110 \rangle$ uniaxial stress [61]. In the presence of TRSB, spontaneous magnetization and currents are generically expected to appear around domain walls, edges, and defects, yet scanning SQUID and Hall probe microscopy [62–69] has failed to find any evidence for them. Josephson junction experiments [57,70–72] show signs of SC domains

---

*grgur.palle@kit.edu

[1]In one sample [53], T_{TRSB} and T_c split even without any external pressure.

TABLE I. Examples of functions transforming according to the irreps of the point group D_{4h} of SRO. D_{4h} is generated by fourfold rotations around z, twofold rotations around x and y, twofold rotations around the diagonals $x \pm y$, and parity. It has five even (A_{1g}, A_{2g}, B_{1g}, B_{2g}, E_g) and five odd (A_{1u}, A_{2u}, B_{1u}, B_{2u}, E_u) irreps, of which E_g and E_u are 2D.

A_{1g}	A_{2g}	B_{1g}	B_{2g}	E_g
$1, x^2 + y^2, z^2$	$xy(x^2 - y^2)$	$x^2 - y^2$	xy	$\{yz \mid -xz\}$
A_{1u}	A_{2u}	B_{1u}	B_{2u}	E_u
$xyz(x^2 - y^2)$	z	xyz	$(x^2 - y^2)z$	$\{x \mid y\}$

in their interference patters, switching behavior, and size dependence of their transport properties, but the domains themselves need not be chiral.

The coupling of SC to strain is partially known from measurements of elastic constants. The main obstacle to making these measurements conclusive is the fact that strain inhomogeneities, such as stacking faults or lattice dislocations, mix elastic waves of different symmetry.[2] That said, according to elastic constant measurements, the SC order appears to couple quadratically to $\varepsilon_{xx} - \varepsilon_{yy} \in B_{1g}$ strain and possibly linearly to $\varepsilon_{xy} \in B_{2g}$ strain. (Irreducible representations (irreps) of SRO are summarized in Table I.) The evidence for the former is the quadratic dependence of T_c on $\varepsilon_{xx} - \varepsilon_{yy}$, whether measured globally [45,73,74] or locally [75], and the absence of a jump at T_c in the shear elastic modulus $C_{B_{1g}} = \frac{1}{2}(C_{11} - C_{12})$ [76–78]. The evidence for the latter is a jump at T_c in the shear elastic constant $C_{66} \in B_{2g}$ [77–79], as measured by ultrasound. However, the magnitude of this jump varies by a factor of 50 between the two experimental groups [77,78] and direct measurements of T_c under [110] strain show linear dependence without any splitting and whose magnitude can be fully accounted without any linear coupling to ε_{xy} [80]. This raises the possibility that the observed jump in C_{66} is due to lattice defect effects that, however, need to be channel selective so as to not generate a jump in $C_{B_{1g}}$. One such proposal [9] is that a subleading pairing channel activates near dislocations; the product of the leading and subleading pairing irreps then determines which elastic modulus experiences a jump. No jump has been observed for the elastic modulus $C_{44} \in E_g$ [76,78], indicating that the coupling to E_g strain is quadratic. Large jumps in the A_{1g} components of the viscosity tensor have recently been discovered at T_c [81].

The preponderance of evidence points towards line nodes. The expected dependence on temperature is found in the heat capacity [82–84], ultrasound attenuation rate [76,85], NMR relaxation rate [24], and London penetration depth [86]. In weak in-plane fields, the heat capacity [84,87] and Knight shift [35] obey Volovik scaling ($\propto \sqrt{B/B_{c2}}$) expected of line nodes [88]. The in-plane thermal conductivity [89,90] exhibits universal transport, which is a type of transport found only in

nodal SC [91–94]. Finally, STM spectroscopy [95,96] shows a V-shaped conductance minimum.[3] The only evidence to the contrary is an STM/S study [97] that scanned micron-sized grains ($\sim 10\,\xi_{ab}$) situated on top of SC aluminium and found an implausibly large SC gap Δ of 3.5 K. Given that so many studies [24,76,82–87] found nodal behavior, in some cases down to as low as 0.04 K $\approx T_c/30$, any fully gapped SC must have extraordinarily deep minima.

The location and orientation of the line node(s) is not settled. Heat capacity [84] and in-plane thermal conductivity [98,99] both display a fourfold anisotropy in their dependence on the in-plane $\boldsymbol{B}$ orientation.[4] Since these anisotropies are small ($\sim 1\,\%$), they can be explained by both horizontal and vertical nodes. That the heat capacity anisotropy has the same sign down to $T_c/20$ appears to exclude d_{xy}-wave pairing [84], and maybe other pairings too. The universal heat transport along c has been found finite with 2σ significance [90], indicating that nodal quasiparticles have a finite c-axis velocity. If true, this result is strong evidence against symmetry-enforced horizontal line nodes. A resonance at transfer energy $\approx 2\Delta$ and momentum with a finite z component was reported below T_c in the inelastic neutron scattering intensity [100], suggesting horizontal line nodes, but was not reproduced in subsequent measurements [101]. In the Fourier transform of the real-space STM tunneling conductance [96], peaks were found at nesting vectors expected of $d_{x^2-y^2}$-wave SC. However, the peaks are not clearly resolved because of noise and compatibility with other pairings was not investigated.

Compelling evidence on SRO's gap structure has recently emerged from measurements performed under uniaxial pressure. When $\langle 100 \rangle$ uniaxial pressure is applied on SRO, its SC is drastically enhanced [45,73,74,102,103], with T_c increasing from 1.5 K to a maximal 3.5 K before decaying again. The most likely cause of this enhancement is the Lifshitz transition that occurs at $\varepsilon_{xx} = -0.44\,\% \equiv \varepsilon_{\mathrm{VH}}$ strain [45,74,104] and is accompanied by an increase in the density of states (DOS). The DOS peaks at $\varepsilon_{\mathrm{VH}}$, as does the normal-state entropy [60]. In the SC state, however, the entropy becomes a *minimum* at $\varepsilon_{\mathrm{VH}}$, as directly measured by the elastocaloric effect [60]. As we later explain, this is only possible if SRO's SC does not have vertical line nodes at the Van Hove lines that induce the DOS peak at $\varepsilon_{\mathrm{VH}}$. This is a severe constraint on possible pairing states, one whose implications we explore in this article. The final piece of the argument is that these properties of strained SRO carry over to the unstrained SC state, which is supported by the absence of any signatures of a bulk SC state change at finite strain in the heat capacity [59], elastocaloric effect [60], or NMR Knight shift [33,35].

The main result of this work is that, among even pairings, only s-wave (A_{1g}), $d_{x^2-y^2}$-wave (B_{1g}), and body-centered periodic $\{d_{xz} \mid d_{yz}\}$-wave (E_g) pairings gap the Van Hove lines. Thus the SC state must include admixtures from at least

---

[2]As pointed out in Ref. [9], dislocations give contributions to elastic constants that are on the order of 1 %, which is two orders of magnitude larger than the (larger of the two sets of) measured jumps of the elastic constants at T_c [78].

---

[3]One should keep in mind that STM mostly probes the α, β bands because of their d_{xz}, d_{yz} orbital characters which make their overlaps with the tip (along z) large.

[4]As pointed out in Ref. [84], little useful information can be extracted from the out-of-plane field-angle anisotropy.

TABLE II. The character table of the point group D_{4h} [112]. Irreps are divided into even (g) and odd (u) ones. C_4 are rotations by $\pm \pi/2$ around the z axis. C_2, C_2', and C_2'' are rotations by π around the z axis, x or y axes, and diagonals $x \pm y$, respectively. P is parity. S_4, Σ_h, Σ_v', Σ_d'' are compositions of C_4, C_2, C_2', C_2'' with P, respectively.

D_{4h}	E	$2C_4$	C_2	$2C_2'$	$2C_2''$	P	$2S_4$	Σ_h	$2\Sigma_v'$	$2\Sigma_d''$
A_{1g}	1	1	1	1	1	1	1	1	1	1
A_{2g}	1	1	1	-1	-1	1	1	1	-1	-1
B_{1g}	1	-1	1	1	-1	1	-1	1	1	-1
B_{2g}	1	-1	1	-1	1	1	-1	1	-1	1
E_g	2	0	-2	0	0	2	0	-2	0	0
A_{1u}	1	1	1	1	1	-1	-1	-1	-1	-1
A_{2u}	1	1	1	-1	-1	-1	-1	-1	1	1
B_{1u}	1	-1	1	1	-1	-1	1	-1	-1	1
B_{2u}	1	-1	1	-1	1	-1	1	-1	1	-1
E_u	2	0	-2	0	0	-2	0	2	0	0

one of these three pairings to be consistent with the elastocaloric experiment. The logic of our argument does not put any constraints on the subleading channels. For instance, almost degenerate states like $d_{x^2-y^2} + i g_{xy(x^2-y^2)}$ [7] or $s' + i d_{xy}$ [14,15] are consistent with a dominant $d_{x^2-y^2}$-wave or s-wave state, respectively. Among odd-parity pairings, all irreps can gap the Van Hove lines. However, A_{2u} and B_{2u} pairings must be made of body-centered periodic wave functions, and for the rest we find nontrivial constraints on the orientations of their Balian-Werthamer $\boldsymbol{d}$-vectors [105].

The paper is organized as follows. In Sec. II, we review some basic properties of SRO. After that, in Sec. III, we explain what has been measured in the elastocaloric experiment [60] and why these measurements forbid vertical line nodes at the Van Hove lines. The precise location of the Van Hove lines is the subject of Sec. IV. Because of its multiband nature, SRO supports a richer set of pairing states than single-band SC [106–108], which is briefly discussed at the beginning of Sec. V and at length in Appendix C. Section V contains the main results of our work: how the momentum and spin-orbit parts of the SC gap behave near the Van Hove lines and which SC states are excluded by the elastocaloric measurements. Table VI is our main result. In the last section, we discuss our results.

II. CRYSTAL AND ELECTRONIC STRUCTURE

SRO is a layered perovskite with a body-centered tetragonal lattice ($a = 3.86$ Å, $c = 12.7$ Å), space group $I4/mmm$, and point group D_{4h} [2,109]. The character table of D_{4h} is given in Table II.

SRO has three conduction bands, conventionally referred to as α, β, and γ, with cylindrical Fermi sheets [2,109]. They are depicted in Fig. 1. These bands primarily derive from the t_{2g} orbital manifold of the Ru atoms, which is made of d_{yz}, d_{zx}, and d_{xy} orbitals [2,20,109]. To a first approximation, due to the high anisotropy, d_{yz} and d_{zx} have 1D tight-binding dispersions:

$$\epsilon_{yz}(\boldsymbol{k}) = -\mu - 2t \cos ak_2, \tag{1}$$
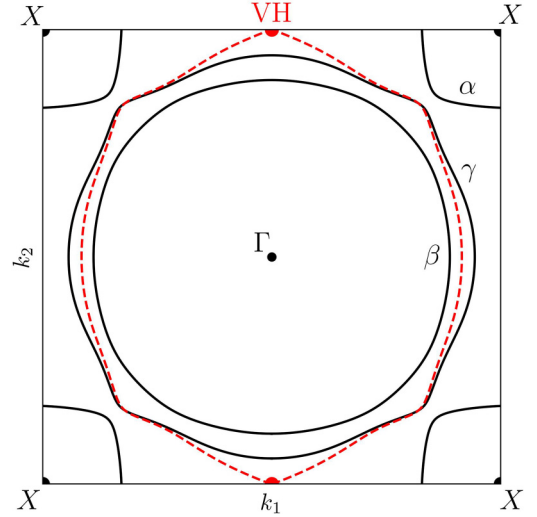
$$\epsilon_{zx}(\boldsymbol{k}) = -\mu - 2t \cos ak_1, \tag{2}$$

FIG. 1. The Fermi surfaces of SRO. The solid black lines are the $k_3 = 0$ cross-sections of the cylindrical α, β, and γ Fermi sheets of unstrained SRO, as determined by our tight-binding model (Appendix B). The dashed red line is the γ band of SRO under Van Hove unaxial strain $\varepsilon_{100} = -0.44\% \equiv \varepsilon_{\text{VH}}$ [60,104]. At this strain, the γ band opens at the Van Hove lines $(0, \pm \frac{\pi}{a}, k_3)$, here denoted with red dots.

whereas d_{xy} has a 2D tight-binding dispersion:

$$\epsilon_{xy}(\boldsymbol{k}) = -\mu - 2t(\cos ak_1 + \cos ak_2)$$
$$- 4t' \cos ak_1 \cos ak_2, \tag{3}$$

where $(\mu, t, t') \approx (0.35, 0.3, 0.1)$ eV [16,110]. After introducing interorbital mixing and spin-orbit coupling, $\epsilon_{yz}(\boldsymbol{k})$ and $\epsilon_{zx}(\boldsymbol{k})$ hybridize into the quasi-1D α and β bands, whereas $\epsilon_{xy}(\boldsymbol{k})$ hybridizes into the quasi-2D γ band (Fig. 1). Interlayer hopping adds warping along k_3. Below 25 K, SRO is a quasi-2D Fermi liquid. Its quasiparticles are strongly renormalized by electronic correlations [2,111]. In the clean limit, SRO develops SC below 1.5 K [2].

Below 25 K, SRO is well-described by a tight-binding model based on the t_{2g} orbitals of ruthenium [16,110,113,114]. Within it, the hopping amplitudes t_δ between neighboring lattice sites are significantly constrained by the symmetries of SRO. In a body-centered lattice, hopping amplitudes along the half-diagonal $\boldsymbol{\delta} = \frac{1}{2}(a\hat{\boldsymbol{e}}_1 + a\hat{\boldsymbol{e}}_2 + c\hat{\boldsymbol{e}}_3)$, as well as many other $\boldsymbol{\delta}$, are additionally possible. However, all such characteristically body-centered hoppings necessarily connect different layers and are thus suppressed by SRO's anisotropy. For the purpose of making estimates, throughout this paper we employ the normal-state model of Ref. [110], the details of which are provided in Appendix B.

III. IMPLICATIONS OF ELASTOCALORIC MEASUREMENTS

The elastocaloric effect describes the change in the temperature that accompanies an adiabatic change in the strain $\varepsilon_{\alpha\beta}$. By measuring it, one may determine the dependence of the entropy S on strain. This is made possible by the thermodynamic
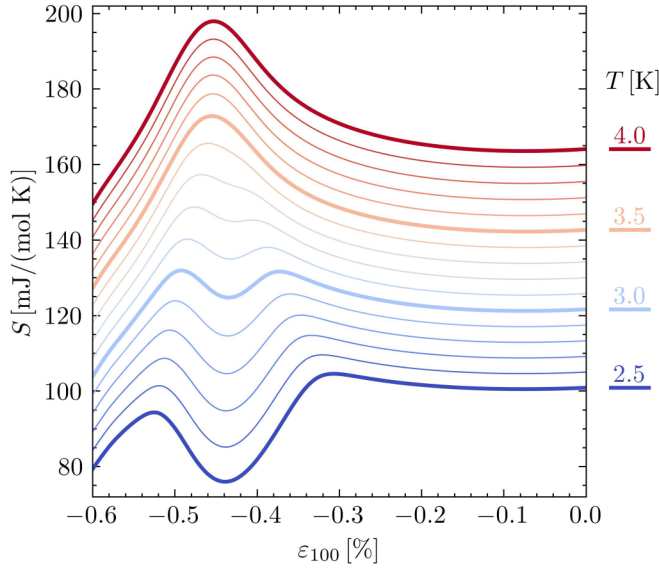
FIG. 2. The entropy S as a function of strain ε_{100} at constant temperatures T ranging from 2.5 (blue) to 4.0 K (red) in 0.1 K increments [119]. The entropies at different temperatures are naturally offset from each other by their temperature dependence. The entropy has been reconstructed from elastocaloric measurements [60] using Eq. (4). At Van Hove strain $\varepsilon_{100} = -0.44\% \equiv \varepsilon_{VH}$, T_c attains its maximal value of 3.5 K. Above (below) 3.5 K, the entropy has a maximum (minimum) at ε_{VH} strain.

identity:

$$\left.\frac{\partial T}{\partial \varepsilon_{\alpha\beta}}\right|_S = -\frac{T}{C_\varepsilon(T)}\left.\frac{\partial S}{\partial \varepsilon_{\alpha\beta}}\right|_T, \tag{4}$$

where $C_\varepsilon(T) = T(\partial S/\partial T)_\varepsilon$ is the heat capacity at constant strain. Recently, important progress has been made in the experimental techniques for measuring the elastocaloric effect and in their analysis for correlated electron systems [115–117].

The elastocaloric effect has been measured last year for strain applied along the [100] direction [60]. Numerical analysis of this dense data set [118] enables the separation of the contribution from C_ε and the reconstruction of the dependence of the entropy on strain [119]; see Fig. 2.

As clearly seen in the figure, the normal-state entropy has a maximum at the Van Hove strain $\varepsilon_{100} = -0.44\% \equiv \varepsilon_{VH}$. As we enter the SC state, however, this maximum becomes a *minimum* as a function of strain. To understand this behavior, let us recall that the entropy of a Fermi liquid is given by [120,121]

$$S = V\frac{\pi^2}{3}k_B^2 T \int dE\, g(E)\delta_T(E), \tag{5}$$

$$\delta_T(E) = \frac{3}{\pi^2 k_B T}[-f \ln f - (1-f)\ln(1-f)], \tag{6}$$

where V is the volume, $g(E)$ the DOS, E is relative to the chemical potential, and $f = 1/(e^{E/k_B T} + 1)$. $\delta_T(E) \to \delta(E)$ as $T \to 0$ so $S \sim Tg(0)$. This formula applies to both the normal and the SC state. Thus to understand the entropy, we need to study the DOS near the Fermi level $E = 0$.

In the normal state, at Van Hove strain the γ band experiences a Lifshitz transition in which its cylindrical Fermi surface opens at the Van Hove lines $\boldsymbol{k}_{VH} \approx (0, \pm\frac{\pi}{a}, k_3)$ along the k_2 direction [45,74,104]. This is shown in Fig. 1. Because of the particularly weak k_3 dispersion of the γ band at $\boldsymbol{k}_{VH}$ ($\sim$1 K), the Van Hove lines contribute a pronounced peak in the DOS that is only rounded on an energy scale of about one kelvin [60]. It is this peak in the DOS that explains the observed normal-state entropy maximum.

To gain a qualitative understanding of what sort of pairings can induce an entropy minimum at ε_{VH} strain, it is sufficient to consider the γ band near the Van Hove lines. This is justified by the fact that the γ band contributes 60 % of the total DOS (Appendix B) and is solely responsible for the normal-state peak in the entropy. For the moment, we shall also neglect the k_3 dispersion.

The DOS of a band in 2D with a dispersion $\epsilon_{\boldsymbol{k}}$ and SC gap $\Delta_{\boldsymbol{k}}$ is given by

$$g_{sc}(E) = 2\int \frac{dk_1\, dk_2}{(2\pi)^2}\delta(E - \xi_{\boldsymbol{k}}), \tag{7}$$

where the 2 is due to spin and $\xi_{\boldsymbol{k}} = \sqrt{\epsilon_{\boldsymbol{k}}^2 + |\Delta_{\boldsymbol{k}}|^2}$ is the Bogoliubov quasiparticle dispersion. It is often easier to calculate the integrated DOS

$$\mathcal{N}_{sc}(E) = \int_0^E dE'\, g_{sc}(E') = 2\int_{\xi_{\boldsymbol{k}} \leqslant E} \frac{dk_1\, dk_2}{(2\pi)^2} \tag{8}$$

and then differentiate it to get $g_{sc}(E)$. Near the Van Hove point $(0, \pi)$, the dispersion of the γ band is approximately given by [see Appendix B or Eq. (18)]:

$$\epsilon_{\boldsymbol{k}} = \frac{1}{2m_1}k_1^2 - \frac{1}{2m_2}k_2^2 = \frac{1}{m_*}q_+ q_-, \tag{9}$$

where $m_* = \sqrt{m_1 m_2} = 1/3200\,\mathrm{K}$, $r = \sqrt[4]{m_2/m_1} = 0.59$, and $q_\pm = \frac{1}{\sqrt{2}}(rk_1 \pm k_2/r)$. Since this expression for $\epsilon_{\boldsymbol{k}}$ only applies near the Van Hove point, we impose a momentum cutoff $|q_\pm| \leqslant \Lambda$.

In the normal state (NS), $\Delta_{\boldsymbol{k}} = 0$ and the DOS at the Van Hove strain equals:

$$g_{sc}^{NS}(E) = \frac{8m_*}{(2\pi)^2}\ln\frac{\Lambda^2}{m_* E}. \tag{10}$$

This diverges logarithmically as $E \to 0$. As we move away from $\varepsilon_{100} = \varepsilon_{VH}$, the logarithmic divergence is moved away from the Fermi level $E = 0$, explaining the normal-state entropy maximum.

If we fully gap (FG) the saddle point, $\Delta_{\boldsymbol{k}} = \Delta_0$, then the DOS vanishes up to Δ_0, $g_{sc}^{FG}(E \leqslant \Delta_0) = 0$, and diverges above it according to ($E > \Delta_0$):

$$g_{sc}^{FG}(E) = \frac{8m_*}{(2\pi)^2}\frac{E}{\sqrt{E^2 - \Delta_0^2}}\ln\frac{\Lambda^2}{m_*\sqrt{E^2 - \Delta_0^2}}. \tag{11}$$

Since $\delta_T(E)$ in Eq. (5) has a width $\sim k_B T$, for sufficiently large $\Delta_0/k_B T$ the normal-state entropy maximum can be suppressed so strongly that it becomes a minimum as a function of strain. Hence fully gapping the Van Hove lines reproduces the features of Fig. 2. Note that a constant gap does not necessarily mean an *s*-wave state, but merely that the gap

is finite in the vicinity of the Van Hove point. For instance, $d_{x^2-y^2}$-wave pairing is finite at the Van Hove point $(0, \pi)$ and approximately constant around it. Our analysis focuses only on the behavior of the pairing gap near the saddle point of the dispersion.

Can pairings with nodal lines at the Van Hove lines also reproduce the SC entropy minimum? To answer this question, let us calculate the DOS for a vertical and horizontal line node. For vertical line nodes (VLN), there are two cases to distinguish: when $\Delta_{\boldsymbol{k}}$ is linear and when $\Delta_{\boldsymbol{k}}$ is quadratic in $\boldsymbol{k}$.

In the linear case, we may always write the gap as

$$\Delta_{\boldsymbol{k}} = \Delta_0(q_+ \cos \varphi + q_- \sin \varphi)/\Lambda = \Delta_0(p_1/\Lambda). \quad (12)$$

In the limit of small E, the inequality $\xi_{\boldsymbol{k}} \leqslant E$ that determines $\mathcal{N}_{sc}(E)$ simplifies to

$$\frac{\Delta_0^2}{\Lambda^2} p_1^2 + \frac{\sin^2(2\varphi)}{4m_*^2} p_2^4 \leqslant E^2, \quad (13)$$

where $p_2 = q_- \cos \varphi - q_+ \sin \varphi$. The area enclosed by this inequality equals $\pi' |p_{1,\max}|_E |p_{2,\max}|_E$, where $\pi' = 4 \int_0^1 dx \sqrt{1 - x^4} \approx 3.496$, and therefore for small E:

$$g_{sc}^{VLN}(E \to 0) = \frac{3\pi'}{(2\pi)^2} \frac{\Lambda}{\Delta_0} \sqrt{\frac{2m_* E}{|\sin 2\varphi|}}. \quad (14)$$

This $g_{sc}^{VLN} \propto \sqrt{E}$ behavior persists up to the point where $g_{sc}^{VLN}(E_w) \approx g_{sc}^{NS}(E_w)$. By solving this equation with $\Delta_0 \sim 3$ K (the T_c at $\varepsilon_{xx} = \varepsilon_{VH}$) and $\Lambda \sim 0.5$, one obtains $E_w \sim 0.2$ K.[5] Exceptionally, when $\varphi = 0$ or $\pi/2$, one finds a constant DOS up to Δ_0:

$$g_{sc}^{VLN'}(E \leqslant \Delta_0) = \frac{8m_*}{(2\pi)^2} \operatorname{arcsinh} \frac{\Lambda^2}{m_* \Delta_0}. \quad (15)$$

Thus if a single line node cuts through the Van Hove point, the DOS generically vanishes like $\sqrt{E}$ in a very narrow range $E \lesssim 0.2$ K. If this line node is fine-tuned to coincide with the lines $q_+ = 0$ or $q_- = 0$, then the DOS becomes finite and large.

The second case is when $\Delta_{\boldsymbol{k}}$ is quadratic in $\boldsymbol{k}$. Quadratic $\Delta_{\boldsymbol{k}}$ may correspond to a line node with a quadratic orthogonal dispersion, a pair of line nodes that intersect at $\boldsymbol{k} = 0$, or a point node, depending on the eigenvalues of the Hessian. The inequality $\xi_{\boldsymbol{k}} \leqslant E$ is in this case invariant under the scaling $\boldsymbol{k} \mapsto \sqrt{\alpha}\boldsymbol{k}$, $E \mapsto \alpha E$. Hence $\mathcal{N}_{sc}(E)$ is linear in E for small E, yielding a finite $g_{sc}^{VLN''}(E = 0)$ and no opening of a gap. Exceptionally, when we have two SC line nodes that coincide with the Van Hove strain Fermi surfaces $q_\pm = 0$, the SC gap equals $\Delta_{\boldsymbol{k}} = \Delta_0(q_+ q_-/\Lambda^2)$, from which we see that $g_{sc}^{VLN''}$ retains the normal-state logarithmic singularity, albeit with a renormalized $1/m_* \mapsto \sqrt{1/m_*^2 + \Delta_0^2/\Lambda^4}$.

Lastly, there's the possibility of a horizontal line node (HLN) crossing the vertical Van Hove line $(0, \pi, k_3)$. For a schematic $\Delta_{\boldsymbol{k}} = \Delta_0(k_3/\pi)$, the 3D DOS can be calculated by
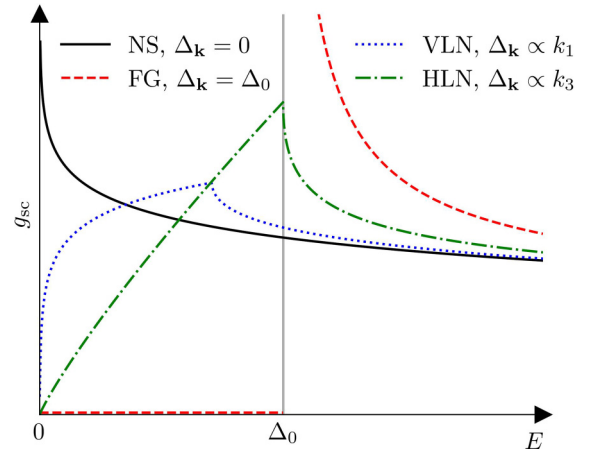

FIG. 3. The Van Hove line contributions to the DOS $g_{sc}(E)$ for the four possible types of gaps considered in the text: normal state (NS), SC with a fully gapped (FG) Van Hove line, SC with a vertical line node (VLN) on the Van Hove line, and SC with a horizontal line node (HLN) crossing the Van Hove line. These correspond to Eqs. (10), (11), (14), and (16), respectively. The VLN case (with $\varphi = \pi/4$) was calculated numerically. The parameter values $m_*^{-1} = 3200$ K, $\Delta_0 = 3$ K, and $\Lambda = 0.5$ were used in all four cases. Note that the Fermi energy ($E = 0$) is tuned precisely to the saddle point, so this depicts the DOS at the Van Hove strain $\varepsilon_{100} = -0.44\%$.

averaging Eq. (11):

$$g_{sc}^{HLN}(E) = \int_{-\pi}^{\pi} \frac{dk_3}{2\pi} g_{sc}^{FG}(E)\big|_{\Delta_0 \to \Delta_0 |k_3|/\pi}$$
$$= \frac{4m_*}{(2\pi)^2} \frac{E}{\Delta_0} \left[\pi \ln \frac{2\Lambda^2}{m_* E} - \zeta(E) \right], \quad (16)$$

where $\zeta(E \leqslant \Delta_0) = 0$ and for $E > \Delta_0$:

$$\zeta(E) = (\pi - 2 \arccos x) \ln \frac{\Lambda^2}{m_* E} + 2 \arcsin x \ln(2x)$$
$$- 2 \arctan \frac{x}{\sqrt{1 - x^2}} \ln x + \operatorname{Cl}_2(\phi), \quad (17)$$

where $x = \sqrt{1 - \Delta_0^2/E^2}$, $\phi = \arccos(1 - 2x^2)$, and $\operatorname{Cl}_2(\phi) = \sum_{k=1}^{\infty} \sin(k\phi)/k^2$ is the Clausen function. g_{sc}^{HLN} is thus roughly linear in E up to Δ_0.

The dependence of the DOS $g_{sc}(E)$ for different realizations of the SC gap $\Delta_{\boldsymbol{k}}$ near the saddle point is summarized in Fig. 3.

Now we come back to the question of whether line nodes at the Van Hove lines are consistent with an entropy minimum. To clarify this issue, we need to take into account the k_3 dispersion, the energy integral in Eq. (5), and the DOS contributions of the other bands.

The k_3 dispersion of the γ band smears all characteristically 2D features of the DOS by the scale of its energy variation $\delta\epsilon_{VH} \sim 2$ K [Eq. (18)]. The normal-state logarithmic singularity becomes a peak. The $g_{sc}^{VLN} \propto \sqrt{E}$ ascent is cut off to give a finite zero-energy DOS that is because of $E_w/\delta\epsilon_{VH} \ll 1$ of the same magnitude as the normal-state DOS. Finally, the HLN DOS attains a finite zero-energy DOS that is at most a factor of three or so smaller than the normal-state DOS (since $\delta\epsilon_{VH}/\Delta_0 \sim 1$). The $\delta_T(E)$ factor in Eq. (5)

---

[5]The solution of $\sqrt{x} = \frac{1}{2}\delta \ln(1/x)$ is $x = \delta^2 W^2(1/\delta)$, where $W(x)$ is the Lambert W-function. In our case, $x = m_* E_w/\Lambda^2$ and $\delta = (8\sqrt{2}/3\pi')(m_* \Delta_0/\Lambda^2)$.

leads to a temperature smearing that has a similar effect: the "effective DOS" that enters the entropy is not $g_{sc}(0)$, but $g_{sc}(E)$ averaged over $E \sim k_B T$. All in all, because of these smearing effects, vertical line nodes at the Van Hove lines $(0, \pm\pi, k_3)$ do not suppress the entropy contribution coming from the Van Hove lines, whereas horizontal line nodes can indeed suppress it.

Because of the strain dependence of T_c, the SC gap becomes ε_{100}-dependent at constant T, peaking at Van Hove strain. A strong enough gapping of the α and β bands could then, in principle, suppress the entropy more than the Van Hove singularities enhance it, resulting in a minimum. To exclude this scenario, we have calculated the entropy for when the α, β, and 80 % of the γ band have $\Delta_{\boldsymbol{k}} = \Delta_0$, and the remaining 20 % of the γ band that includes the Van Hove lines has $\Delta_{\boldsymbol{k}} = 0$ [122]. The result of this calculation is that a minimum as a function of strain does develop, but the drop in the entropy is 20 % too small when compared to experiment at 2.5 K. Thus even in this worst-case scenario, where line nodes that are known [24,76,82–87] to be present in the system are neglected, the Van Hove lines must be gapped in some way to agree with experiment.

The final conclusion that follows from all of these considerations is that the Van Hove lines $\boldsymbol{k}_{VH} \approx (0, \pm\frac{\pi}{a}, k_3)$ must be either fully gapped or can at most have a horizontal line node crossing them. Hence, we may exclude vertical line nodes at $\boldsymbol{k}_{VH}$ near Van Hove strain [60]. That the heat capacity jump is maximal at the Van Hove strain [59] also supports this conclusion. Vertical line nodes away from the Van Hove lines are still possible.

To draw conclusions for the unstrained tetragonal system from measurements performed at uniaxial strain $\varepsilon_{100} \approx \varepsilon_{VH}$, we rely on the assumption that the pairing states of the strained and unstrained system are adiabatically connected. Measurements of the highly-sensitive elastocaloric effect [60] and heat capacity [59] show no hints of a transition between two different bulk SC states under [100] strain. By contrast, the onset of spin-density waves, previously found through muon spin relaxation [53], is clearly visible in the elastocaloric data of Ref. [60]. So the elastocaloric effect is able to identify a variety of phase transitions.

We may thus exclude all SC states of the unstrained system that are adiabatically connected to SC states of the ε_{xx} strained system which have a vertical line node at $\boldsymbol{k}_{VH} \approx (0, \pm\frac{\pi}{a}, k_3)$. Given that ε_{xx} strain preserves all the symmetry operations that map the Van Hove lines to themselves, as we shall see in Sec. V, we may conclude that there are no vertical line nodes at either $(\pm\frac{\pi}{a}, 0, k_3)$ nor $(0, \pm\frac{\pi}{a}, k_3)$ in the unstrained tetragonal system. Intuitively, this means that SRO's SC takes full advantage of the enhanced DOS induced by the Van Hove lines. Indeed, the drastic enhancement of T_c and B_{c2} under uniaxial pressure [45,73,74,102,103] were suggestive of this conclusion long ago, but only with the recent elastocaloric measurements of Ref. [60] could more conclusive statements be made.

IV. LOCATION OF THE VAN HOVE LINES

Here we establish that the Van Hove lines are adequately approximated with $(\pm\frac{\pi}{a}, 0, k_3)$ and $(0, \pm\frac{\pi}{a}, k_3)$. For a simple-

tetragonal lattice, the Van Hove lines are lines of high symmetry. However, they are not located precisely on the boundary of the body-centered first Brillouin zone relevant here, which could in principle allow for large deviations away from $(\pm\frac{\pi}{a}, 0, k_3)$ and $(0, \pm\frac{\pi}{a}, k_3)$. As we shall see, the high anisotropy of SRO makes these deviations negligible, justifying the subsequent analysis.

Van Hove points are points in momentum space where the gradient of the band energy $\epsilon_{\boldsymbol{k}}$ vanishes. In 3D, the solutions of $\nabla\epsilon_{\boldsymbol{k}} = \boldsymbol{0}$ are generically isolated points. However, quasi-2D dispersions may yield Van Hove *lines*, that is, lines on which a number of Van Hove points are situated of similar energy. The quality of the emergent Van Hove lines is quantified by how well-aligned the Van Hove points are to a line and by how close the energies of the Van Hove points are.

Consider the Van Hove line $(0, \frac{\pi}{a}, k_3)$. Then for any two $\boldsymbol{k} = (\delta k_1, \frac{\pi}{a} + \delta k_2, k_3)$ and $\boldsymbol{k}' = R(g)\boldsymbol{k}$ related by a symmetry operation $g \in D_{4h}$, $\epsilon_{\boldsymbol{k}} = \epsilon_{\boldsymbol{k}'+\boldsymbol{K}}$ for any reciprocal lattice vector $\boldsymbol{K}$. Applying this to parity gives $\nabla\epsilon_{\boldsymbol{k}} = \boldsymbol{0}$ at the midpoints of the Brillouin zone faces, which for body-centered tetragonal SRO are $(0, \frac{\pi}{a}, \pm\frac{\pi}{c})$. These are the first two Van Hove points. The positions of the other two Van Hove points are restricted by symmetry to be at $(0, \frac{\pi}{a} + \delta k_{VH,2}, 0)$ and $(0, \frac{\pi}{a} - \delta k_{VH,2}, \pm\frac{2\pi}{c})$. Reflection across the $k_1 = 0$ plane implies $\partial_{k_1}\epsilon_{\boldsymbol{k}} = 0$ in the $k_1 = 0$ plane and reflection across the $k_3 = 0$ plane implies $\partial_{k_3}\epsilon_{\boldsymbol{k}} = 0$ in the planes $k_3 = 0, \pm\frac{2\pi}{c}$. If the system were simple-tetragonal-periodic, then reflection across the $k_2 = 0$ plane would imply $\partial_{k_2}\epsilon_{\boldsymbol{k}} = 0$ in the $k_2 = \pm\frac{\pi}{a}$ planes, making $\delta k_{VH,2} = 0$. Because of the smallness of the characteristically body-centered hopping in SRO, which is always between layers, $\delta k_{VH,2}$ is very close to zero.

From the tight-binding model (Appendix B), we may extract the following simplified expression for the dispersion of the γ band near the Van Hove line $(0, \frac{\pi}{a}, k_3)$:

$$\epsilon_{\boldsymbol{k}} = \mu_{VH} + \frac{a^2}{2m_1}k_1^2 - \frac{a^2}{2m_2}\left(k_2 - \frac{\pi}{a}\right)^2$$
$$- \delta\epsilon_{VH}\cos ck_3 + \frac{a^2}{m_2}\delta k_{VH,2}\left(k_2 - \frac{\pi}{a}\right)\cos\frac{ck_3}{2}. \quad (18)$$

Its form follows from symmetry; only the lowest powers in k_1, k_2 and lowest harmonics in k_3 were retained. Here $\mu_{VH} = 54$ meV, $\delta\epsilon_{VH} = 2.4$ K, $\delta k_{VH,2} = 0.013/a$, $m_1^{-1} = 1100$ K, and $m_2^{-1} = 9300$ K. While this dispersion was derived from a model of unstrained SRO, it offers a good understanding of the effects of the k_3-dispersion on the Van Hove line. The deviation of the Van Hove points from the $(\frac{\pi}{a}, 0, k_3)$-line is characterized by $\delta k_{VH,2} \ll \frac{2\pi}{a}$, which is a factor of 500 smaller than the width of the Brillouin zone. Furthermore, the difference in the γ band energies of the Van Hove points is given by $\delta\epsilon_{VH}$ which is on the order of a few kelvins. We may thus conclude that the four Van Hove points, illustrated in Fig. 4, together constitute a Van Hove line $(0, \frac{\pi}{a}, k_3)$ to a high degree of accuracy. The same is true for the Van Hove lines $(0, -\frac{\pi}{a}, k_3)$ and $(\pm\frac{\pi}{a}, 0, k_3)$.

V. BEHAVIOR ON THE VAN HOVE LINES

To see which SC states are excluded by the fact that vertical line nodes on the Van Hove lines are incompatible with the

(a) 3D Brillouin zone

(b) $k_1 = 0$ cross-section
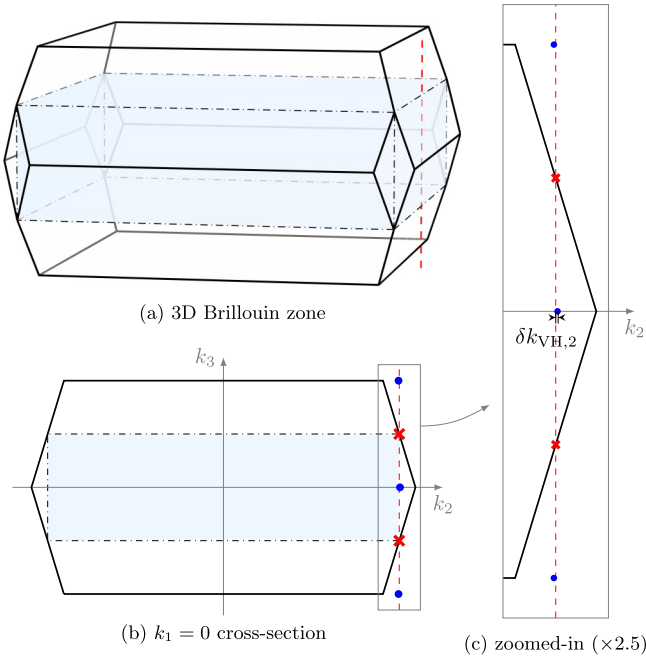
(c) zoomed-in ($\times 2.5$)

FIG. 4. The body-centered tetragonal Brillouin zone of SRO (a), its $k_1 = 0$ cross-section (b), and the region around the $(0, \frac{\pi}{a}, k_3)$ Van Hove line (c). Shaded in blue is the simple tetragonal Brillouin zone. The red crosses are the $(0, \frac{\pi}{a}, \pm\frac{\pi}{c})$ Van Hove points. The blue dots are the $(0, \frac{\pi}{a} + \delta k_{\mathrm{VH},2}, 0)$ and $(0, \frac{\pi}{a} - \delta k_{\mathrm{VH},2}, \pm\frac{2\pi}{c})$ Van Hove points. Together they constitute the Van Hove line $(0, \frac{\pi}{a}, k_3)$, drawn here with a dashed red line. The displacement length $\delta k_{\mathrm{VH},2} \approx 0.013/a$ is designated in (c).

elastocaloric effect data, we first need to see which SC states are possible. This is significant because the multiband nature of SRO allows for a richer set of possibilities than usual. Since this has already been analyzed [106–108], here we only briefly discuss how the multiband case differs from the singleband one, delegating the details of the categorization of all possible SC states to Appendix C.

To describe SRO's SC, we employ an effective model based on the t_{2g} orbitals of Ru (Appendix B). Within it, SC is described by a gap matrix $\Delta_{\alpha\beta}(\boldsymbol{k})$ which is characterized by its momentum dependence and spin-orbit structure. It is the possibility of a nontrivial orbital structure that sets multiband systems apart from singleband ones. Thus, for instance, when dealing with even pairings, we cannot simply assume a spin singlet that transforms trivially (A_{1g}) under all symmetry operations and equate the irrep of the momentum wave function with the irrep of the total gap matrix. The irrep of the gap matrix is determined by the *product* of the irreps of its momentum and spin-orbit parts. Within the effective model, there are spin-orbit matrices belonging to all the possible irreps of D_{4h} for both even and odd pairings. The details of how $\Delta_{\alpha\beta}(\boldsymbol{k})$ are constructed by combining pairing wave functions $d(\boldsymbol{k})$ with spin-orbit matrices Γ can be found in Appendix C.

Now we analyze which SC states of the ε_{xx} strained system gap the Van Hove lines sufficiently strongly to be able to explain the elastocaloric experiment [60]. Viable unstrained SC states must be adiabatically connected to these states. As we shall see, in the arguments of this section the key

TABLE III. The character table of the point group D_{2h} [112]. Irreps are divided into even (g) and odd (u) ones. Primes have been added on the irreps to distinguish them from D_{4h} irreps. C_2^x, C_2^y, and C_2^z are rotations by π around the x, y, and z axes, respectively. P is parity. Σ_x, Σ_y, Σ_z are compositions of C_2^x, C_2^y, and C_2^z with P, respectively.

D_{2h}	E	C_2^z	C_2^y	C_2^x	P	Σ_z	Σ_y	Σ_x
A_{1g}'	1	1	1	1	1	1	1	1
B_{1g}'	1	1	−1	−1	1	1	−1	−1
B_{2g}'	1	−1	1	−1	1	−1	1	−1
B_{3g}'	1	−1	−1	1	1	−1	−1	1
A_{1u}'	1	1	1	1	−1	−1	−1	−1
B_{1u}'	1	1	−1	−1	−1	−1	1	1
B_{2u}'	1	−1	1	−1	−1	1	−1	1
B_{3u}'	1	−1	−1	1	−1	1	1	−1

symmetry operations are those that map the Van Hove lines $\boldsymbol{k}_{\mathrm{VH}} = (0, \pm\frac{\pi}{a}, k_3)$ to themselves. As it turns out, although ε_{xx} strain reduces the point group from D_{4h} to D_{2h} (Table III), the symmetries that map the Van Hove lines to themselves are the same for both D_{4h} and D_{2h}. Hence we may do the whole analysis either with or without ε_{xx} strain. We have opted for the latter. Using Table IV, one may translate all the results for irreps of D_{4h} of this section into results for irreps of D_{2h}. Table IV also specifies which irreps of D_{2h} are adiabatically connected to which irreps of D_{4h}, which brings us back to the initial D_{4h} irreps.

Let us consider the Van Hove line $\boldsymbol{k}_{\mathrm{VH}} = (0, \frac{\pi}{a}, k_3)$. For a SC gap matrix $\Delta_a(\boldsymbol{k})$ to be able to gap the γ band at $\boldsymbol{k}_{\mathrm{VH}}$, both its pairing wave function $d_a(\boldsymbol{k})$ and the projection of its spin-orbit matrix Γ_a onto the γ band must be finite there.

The only point group symmetries $g \in D_{4h}$ that constrain $d_a(\boldsymbol{k}_{\mathrm{VH}})$ or the band projections of Γ_a are those that map the $(0, \frac{\pi}{a}, k_3)$ line to itself, modulo body-centered reciprocal lattice vectors. One readily find that these are

$$\Sigma_x' : k_3 \mapsto k_3,$$

$$\Sigma_y', C_{2z} : k_3 \mapsto k_3 + \frac{2\pi}{c},$$

$$\Sigma_h, C_{2y}' : k_3 \mapsto -k_3,$$

$$C_{2x}' : k_3 \mapsto -k_3 + \frac{2\pi}{c}. \qquad (19)$$

Here, C_{2x}', C_{2y}', C_{2z} are rotations by π around x, y, and z, respectively, and $\Sigma_x' = PC_{2x}'$, $\Sigma_y' = PC_{2y}'$, $\Sigma_h = PC_{2z}$ are re-

TABLE IV. Reduction of the D_{4h} irreps (top) to D_{2h} irreps (bottom) that occurs under ε_{xx} uniaxial strain. Parity stays the same so we have suppressed the g/u subscripts. $\{x \mid y\}$ transforms according to the $\rho^{(E)}(g)$ of Eq. (C4), Appendix C.

D_{4h}: $A_1\{x\}$ $B_1\{x\}$ $A_2\{x\}$ $B_2\{x\}$ $E\{x \mid y\}$

D_{2h}: $A_1'\{x\}$ $B_1'\{x\}$ $B_2'\{y\}$ $B_3'\{x\}$

TABLE V. The $\rho_{ab}^{(\lambda)}(g)$ of nontrivial irreps λ of D_{4h}.

g	A_{2g}	B_{1g}	B_{2g}	E_g	A_{1u}	A_{2u}	B_{1u}	B_{2u}	E_u
Σ'_x	-1	1	-1	$\begin{pmatrix} 1 & 0 \\ 0 & -1 \end{pmatrix}$	-1	1	-1	1	$\begin{pmatrix} -1 & 0 \\ 0 & 1 \end{pmatrix}$
Σ'_y	-1	1	-1	$\begin{pmatrix} -1 & 0 \\ 0 & 1 \end{pmatrix}$	-1	1	-1	1	$\begin{pmatrix} 1 & 0 \\ 0 & -1 \end{pmatrix}$
Σ_h	1	1	1	$\begin{pmatrix} -1 & 0 \\ 0 & -1 \end{pmatrix}$	-1	-1	-1	-1	$\begin{pmatrix} 1 & 0 \\ 0 & 1 \end{pmatrix}$
C'_{2x}	-1	1	-1	$\begin{pmatrix} 1 & 0 \\ 0 & -1 \end{pmatrix}$	1	-1	1	-1	$\begin{pmatrix} 1 & 0 \\ 0 & -1 \end{pmatrix}$

flections. Given that $C_{2z} = \Sigma'_x \Sigma'_y$ and $C'_{2y} = \Sigma'_x \Sigma_h$, we may focus solely on the reflections and C'_{2x}. Their matrices are listed in Table V. The strongest constraints follow from Σ'_x because it maps $k_3 \mapsto k_3$. In the simple tetragonal limit, $k_3 \cong k_3 + \frac{2\pi}{c}$ so $\boldsymbol{k}_{\text{VH}}$ are on the Brillouin zone boundary and Σ'_y, C_{2z} give strong constraints too.

Consider one of the four g from Table V and a k_3 that g maps to itself, modulo $\frac{4\pi}{c}$. Periodicity and the symmetry transformation rule of pairing wave functions [Eq. (C5), Appendix C] then give the constraint:

$$d_a\left(0, \frac{\pi}{a}, k_3\right) = \sum_{b=1}^{\dim \lambda} \rho_{ab}^{(\lambda)}(g) d_b\left(0, \frac{\pi}{a}, k_3\right). \qquad (20)$$

By analyzing it, we find the following symmetry-enforced behavior of $d_a(0, \frac{\pi}{a}, k_3)$, depending on its irrep and k_3.

(i) d belonging to $A_{2g}, B_{2g}, A_{1u},$ and B_{1u} vanish for all k_3.

(ii) For $\{d_1 \mid d_2\} \in E_g$, d_2 vanishes for all k_3, whereas d_1 vanishes only at $k_3 = 0, \pm\frac{2\pi}{c}$.

(iii) For $\{d_1 \mid d_2\} \in E_u$, d_1 vanishes for all k_3, whereas d_2 vanishes only at $k_3 = \pm\frac{\pi}{c}$.

(iv) For those $\{d_1 \mid d_2\} \in E_{g/u}$ that are periodic under simple tetragonal translations ($k_3 \cong k_3 + \frac{2\pi}{c}$), both components vanish for all k_3.

(v) d from irreps A_{2u} and B_{2u} vanish only at $k_3 = 0, \pm\frac{\pi}{c}$, and $\pm\frac{2\pi}{c}$, but are otherwise unconstrained.

(vi) d from A_{1g} and B_{1g} are completely unconstrained for all k_3.

To proceed, we consider the pairing of the band eigenstates of the problem and focus on intraband pairing. To find it, we need to project Γ_a onto the bands. Call $V_{\boldsymbol{k}} = (v_{\boldsymbol{k}\uparrow}, v_{\boldsymbol{k}\downarrow})$ the Kramers-degenerate eigenvectors of the γ band, $H_{\boldsymbol{k}} V_{\boldsymbol{k}} = \epsilon_{\boldsymbol{k}} V_{\boldsymbol{k}}$. The projection is then given by

$$P_{\boldsymbol{k}a} = V_{\boldsymbol{k}}^\dagger \Gamma_a V_{-\boldsymbol{k}}^* = \sum_\mu P_a^\mu(\boldsymbol{k}) \sigma_\mu(\mathrm{i}\sigma_y), \qquad (21)$$

where the Pauli matrices act in pseudospin space. Since all three t_{2g} orbitals are even, we may locally choose a gauge in which $V_{-\boldsymbol{k}} = V_{\boldsymbol{k}}$ so that $P_{\boldsymbol{k}a}^{\mathsf{T}} = sP_{-\boldsymbol{k}a} = sP_{\boldsymbol{k}a}$, where $\Gamma_a^{\mathsf{T}} = s\Gamma_a$. $\mu = 0$ for antisymmetric Γ_a ($s = -1$), whereas $\mu \in \{x, y, z\}$ for symmetric Γ_a ($s = +1$).

Whenever a $g \in D_{4h}$ maps a $\boldsymbol{k}$ to itself modulo periodicity, its symmetry transformation matrix $U(g) = M(g) \otimes S(g)$ (Appendix B, Table VII) commutes with the normal-state Hamiltonian $H_{\boldsymbol{k}}$:

$$U^\dagger(g) H_{\boldsymbol{k}} U(g) = H_{R(g^{-1})\boldsymbol{k}} = H_{\boldsymbol{k}}. \qquad (22)$$

This means that the interband parts of $U(g)$ vanish. As for the intraband part, we may always choose a basis for the Kramers degenerate subspace such that it takes a spin-like form:

$$V_{\boldsymbol{k}}^\dagger U(g) V_{\boldsymbol{k}} = S(g). \qquad (23)$$

The symmetry transformation rule of spin-orbit matrices [Eq. (C6), Appendix C] now gives the constraint:

$$S^\dagger(g) P_{\boldsymbol{k}a} S^*(g) = \sum_{b=1}^{\dim \lambda} \rho_{ab}^{(\lambda)}(g) P_{\boldsymbol{k}b}. \qquad (24)$$

For $\boldsymbol{k}$ on the Van Hove line $(0, \frac{\pi}{a}, k_3)$, the g from Table V constrain certain $P_a^\mu(\boldsymbol{k})$ to vanish, depending on the (anti)symmetry, irrep, and k_3. The (anti)symmetry $\Gamma_a^{\mathsf{T}} = s\Gamma_a$ we shall denote with an irrep superscript $s = \pm$. Thus, for instance, $\Gamma \in A_{1g}^-$ are antisymmetric under transposition, whereas $\Gamma \in B_{1g}^+$ are symmetric under transposition. The symmetry-enforced behavior of $P_a^\mu(0, \frac{\pi}{a}, k_3)$ we may summarize as follows.

(i) Γ belonging to A_{2g}^- and B_{2g}^- have $P^0 = 0$ for all k_3.

(ii) $\{\Gamma_1 \mid \Gamma_2\} \in E_g^-$ have $P_2^0 = 0$ for all k_3, whereas $P_1^0 = 0$ only at $k_3 = 0, \pm\frac{2\pi}{c}$.

(iii) $\Gamma \in A_{1g}^+, B_{1g}^+$ have $P^y = P^z = 0$ for all k_3, and $P^x = 0$ only at $k_3 = 0, \pm\frac{2\pi}{c}$.

(iv) $\Gamma \in A_{2g}^+, B_{2g}^+$ have $P^x = 0$ for all k_3, and $P^y = 0$ only at $k_3 = 0, \pm\frac{2\pi}{c}$. P^z is unconstrained.

(v) $\{\Gamma_1 \mid \Gamma_2\} \in E_g^+$ have $P_1^y = P_1^z = P_2^z = 0$ for all k_3, and $P_2^z = 0$ only at $k_3 = 0, \pm\frac{2\pi}{c}$. The remaining P_1^x and P_2^y are unconstrained.

(vi) The P^0 of Γ from A_{1g}^- and B_{1g}^- are completely unconstrained for all k_3.

In the limit of vanishing body-centered tetragonal hopping, the following P_a^μ vanish in addition.

(i) For $\{\Gamma_1 \mid \Gamma_2\} \in E_g^-$, P_1^0 vanishes for all k_3 so both P_a^0 are zero.

(ii) For $\Gamma \in A_{1g}^+, B_{1g}^+$, P^μ completely vanish for all k_3.

(iii) For $\Gamma \in A_{2g}^+, B_{2g}^+$, $P^y = 0$ for all k_3, but P^z is still unconstrained.

(iv) For $\{\Gamma_1 \mid \Gamma_2\} \in E_g^+$, $P_2^z = 0$ for all k_3, but P_1^x and P_2^y are still unconstrained.

Owning to the fact that all characteristically body-centered hopping is necessarily between layers and that these hoppings are very small in SRO because of its high anisotropy, the vanishing P_a^μ listed above are very small for SRO, although not precisely zero. Using the tight-binding model of Ref. [110], described in Appendix B, we have quantified their smallness: the vanishing P_a^μ listed above are by a factor of 50 or more smaller than the largest possible $P_a^\mu \sim 1$, where all Γ_a have been normalized to $\mathrm{tr}\Gamma_a^\dagger \Gamma_a = 1$ for a fair comparison.

Unlike the above anisotropy argument, arguments based on the d_{xy} orbital character of the γ band do not suppress any irreps, but only inform us on which Γ_a from within a given irrep have large P_a^μ.

Finally, we synthesize the results found for d_a and Γ_a. This is done by going through the multiplication table of irreps (Table XI in Appendix C) and seeing which entries yield a $\Delta_a(\boldsymbol{k})$ with a finite γ band projection. The results are summarized in Table VI. Table VI is the main result of this paper.

TABLE VI. Even-parity (a) and odd-parity (b) pairings that do not have a vertical line node at $(0, \frac{\pi}{a}, k_3)$, constructed by combining pairing wave functions $d_a(\boldsymbol{k})$ with spin-orbit matrices Γ_a according to the multiplication table of D_{4h} irreps (Table XI, Appendix C). A "+" superscript on a spin-orbit matrix irrep means that the matrices are symmetric ($\Gamma^{\mathsf{T}} = +\Gamma$), whereas a "−" superscript indicates antisymmetry under transposition. A zero component of $E_{g/u}$ means that it vanishes on $(0, \frac{\pi}{a}, k_3)$. Highlighted red are those d_a that must be periodic under body-centered translations, but not under simple tetragonal translations, to be finite on $(0, \frac{\pi}{a}, k_3)$. For examples, see Table IX from Appendix C. Such d_a have horizontal line nodes at $k_3 = 0, \pm\frac{2\pi}{c}$. Highlighted blue are those Γ_a whose projections onto the γ band are suppressed by two orders of magnitude because of the weakness of body-centered interlayer hopping. Such Γ_a are unable to account for the elastocaloric experiment, but are listed for the sake of completeness.

$\otimes$	$A_{1g}\{d\}$	$B_{1g}\{d\}$	$E_g\{d_1 \mid 0\}$
$A_{1g}^-\{\Gamma\}$	$A_{1g}\{\Gamma d\}$	$B_{1g}\{\Gamma d\}$	$E_g\{\Gamma d_1 \mid 0\}$
$B_{1g}^-\{\Gamma\}$	$B_{1g}\{\Gamma d\}$	$A_{1g}\{\Gamma d\}$	$E_g\{\Gamma d_1 \mid 0\}$
$E_g^- \left\{ \begin{smallmatrix} \Gamma_1 \\ 0 \end{smallmatrix} \right\}$	$E_g\left\{\begin{smallmatrix}\Gamma_1 d \\ 0\end{smallmatrix}\right\}$	$E_g\left\{\begin{smallmatrix}\Gamma_1 d \\ 0\end{smallmatrix}\right\}$	$A_{1g}\{\Gamma_1 d_1 + 0\}$ $\oplus B_{1g}\{\Gamma_1 d_1 - 0\}$

(a) Even pairings that are finite on $(0, \frac{\pi}{a}, k_3)$.

$\otimes$	$A_{2u}\{d\}$	$B_{2u}\{d\}$	$E_u\{0 \mid d_2\}$
$A_{1g}^+\{\Gamma\}$	$A_{2u}\{\Gamma d\}$	$B_{2u}\{\Gamma d\}$	$E_u\{0 \mid \Gamma d_2\}$
$A_{2g}^+\{\Gamma\}$	$A_{1u}\{\Gamma d\}$	$B_{1u}\{\Gamma d\}$	$E_u\{\Gamma d_2 \mid 0\}$
$B_{1g}^+\{\Gamma\}$	$B_{2u}\{\Gamma d\}$	$A_{2u}\{\Gamma d\}$	$E_u\{0 \mid -\Gamma d_2\}$
$B_{2g}^+\{\Gamma\}$	$B_{1u}\{\Gamma d\}$	$A_{1u}\{\Gamma d\}$	$E_u\{\Gamma d_2 \mid 0\}$
$E_g^+ \left\{ \begin{smallmatrix} \Gamma_1 \\ \Gamma_2 \end{smallmatrix} \right\}$	$E_u\left\{\begin{smallmatrix}\Gamma_2 d \\ -\Gamma_1 d\end{smallmatrix}\right\}$	$E_u\left\{\begin{smallmatrix}\Gamma_2 d \\ \Gamma_1 d\end{smallmatrix}\right\}$	$A_{1u}\{0 + \Gamma_2 d_2\}$ $\oplus A_{2u}\{\Gamma_1 d_2 - 0\}$ $\oplus B_{1u}\{0 - \Gamma_2 d_2\}$ $\oplus B_{2u}\{\Gamma_1 d_2 + 0\}$

(b) Odd pairings that are finite on $(0, \frac{\pi}{a}, k_3)$.

As mentioned, SRO's anisotropy suppresses the blue entries of the table by two orders of magnitude. This means that a Δ with a maximal value $\sim k_B T_c$ is way too small on the Van Hove lines to explain the observed entropy quenching [60]. Hence the blue entries of Table VI are excluded as possible leading SC states as well.

From Table VI we see that, among even pairings, only A_{1g}, B_{1g}, and E_g irreps have pairings that do not have symmetry-enforced vertical line nodes on the Van Hove lines. Thus even pairings must have admixtures from one of these three irreps to be able to explain the elastocaloric experiment of Ref. [60]. It is worth noting that within these three irreps, pairings with symmetry-enforced vertical line nodes on $\boldsymbol{k}_{\mathrm{VH}}$ do exist, like for instance $\Delta(\boldsymbol{k}) = \Lambda_1(\mathrm{i}\sigma_y)\sin ak_1 \sin ak_2 \in B_{2g}^- \otimes B_{2g} = A_{1g}$ (Λ_1 is given in Appendix A). So Table VI also yields nontrivial information on the spin-orbit and momentum structure of these Van Hove line-gapping admixtures. Three representatives of such even-parity $\boldsymbol{k}_{\mathrm{VH}}$-gapping SC states are plotted in Fig. 5.

One such piece of information is that E_g pairing must be made of wave functions d_a that are body-centered periodic, but not simple tetragonal periodic. The lowest order such
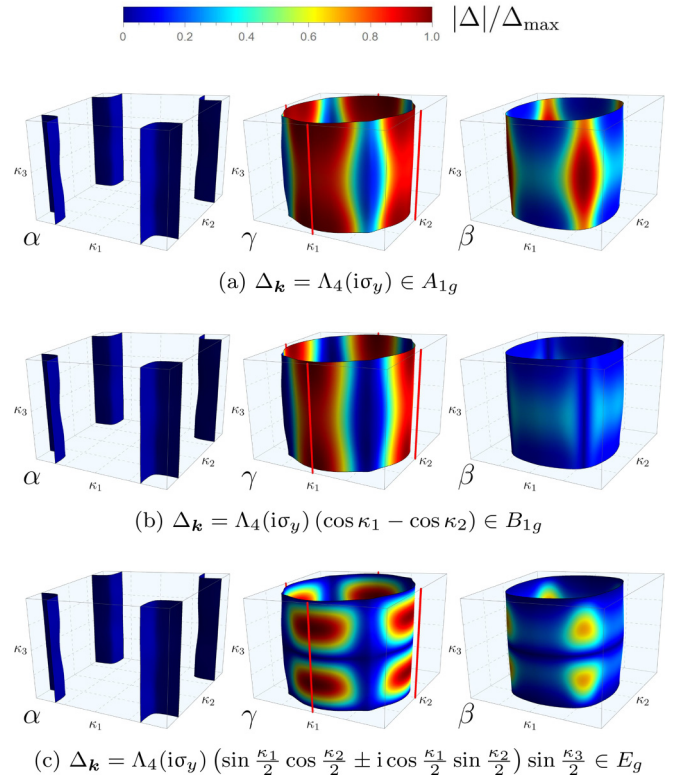

(a) $\Delta_{\boldsymbol{k}} = \Lambda_4(\mathrm{i}\sigma_y) \in A_{1g}$

(b) $\Delta_{\boldsymbol{k}} = \Lambda_4(\mathrm{i}\sigma_y)(\cos\kappa_1 - \cos\kappa_2) \in B_{1g}$

(c) $\Delta_{\boldsymbol{k}} = \Lambda_4(\mathrm{i}\sigma_y)\left(\sin\frac{\kappa_1}{2}\cos\frac{\kappa_2}{2} \pm \mathrm{i}\cos\frac{\kappa_1}{2}\sin\frac{\kappa_2}{2}\right)\sin\frac{\kappa_3}{2} \in E_g$

FIG. 5. Projections onto the Fermi sheets of three Van Hove line-gapping SC states $\Delta_{\boldsymbol{k}}$ from Table VI, belonging to irreps A_{1g} (a), B_{1g} (b), and chiral E_g (c), respectively. $\kappa_1 = ak_1 \in [-\pi, \pi]$, $\kappa_2 = ak_2 \in [-\pi, \pi]$, and $\kappa_3 = ck_3 \in [-2\pi, 2\pi]$. In the γ sheet plots, the Van Hove lines $(\pm\frac{\pi}{a}, 0, k_3)$ and $(0, \pm\frac{\pi}{a}, k_3)$ are highlighted red. Because of the $\Lambda_4 = \mathrm{diag}(0, 0, \sqrt{2})$ orbital structure we have chosen, the projections are only large where the bands have d_{xy} orbital character, which is on the γ sheet and where the γ and β sheets nest. More plots can be found in Appendix D.

$\{d_{xz} \mid d_{yz}\} \in E_g$ is

$$\left\{ \sin\frac{ak_1}{2}\cos\frac{ak_2}{2}\sin\frac{ck_3}{2} \,\middle|\, \cos\frac{ak_1}{2}\sin\frac{ak_2}{2}\sin\frac{ck_3}{2} \right\}. \quad (25)$$

It is this pairing state, only allowed because of the body-centered tetragonal structure of SRO, that opens a gap at the Van Hove line and that we cannot exclude based on the elastocaloric data. In Ref. [16], it was shown that such a pairing state can be stabilized by a strongly momentum-dependent spin-orbit coupling. A better understanding of the origin of such momentum dependence might help elucidate whether this state is a viable option for SRO's SC. In distinction, the E_g pairing state

$$\{\sin ak_1 \sin ck_3 \mid \sin ak_2 \sin ck_3\}, \quad (26)$$

which would be the only allowed one for simple-tetragonal lattices, cannot be the only pairing state as it does not open a gap on the Van Hove line. An important difference between these two types of states [(25) vs. (26)] is that the former always have horizontal line nodes at $k_3 = 0, \pm\frac{2\pi}{c}$.

Among odd pairings, all irreps have pairings without symmetry-enforced vertical line nodes on $\boldsymbol{k}_{\mathrm{VH}}$. However, the orientations of the Balian-Werthamer $\boldsymbol{d}$-vectors [105] are non-

trivially restricted and the nonsuppressed A_{2u} and B_{2u} pairings are necessarily made of characteristically body-centered periodic d_a.

In multiband systems with spin-orbit coupling, a $\boldsymbol{d}$-vector is associated with each band in its pseudospin (Kramers) space. It is defined through

$$V_{\boldsymbol{k}n}^{\dagger}\Delta(\boldsymbol{k})V_{-\boldsymbol{k}n}^{*} = \boldsymbol{d}_{\boldsymbol{k}n} \cdot \boldsymbol{\sigma}(i\sigma_y), \tag{27}$$

where $V_{\boldsymbol{k}n} = (v_{\boldsymbol{k}n\uparrow}, v_{\boldsymbol{k}n\downarrow})$ are the Kramers-degenerate eigenvectors of the nth band and $V_{-\boldsymbol{k}n} = V_{\boldsymbol{k}n}$. We make the following gauge choice for the pseudospins:

$$\begin{aligned}
V_{\boldsymbol{k}n}^{\dagger}(\mathbb{1} \otimes i\sigma_y)V_{\boldsymbol{k}n}^{*} &= i\sigma_y, \\
V_{\boldsymbol{k}n}^{\dagger}(\mathbb{1} \otimes \sigma_z)V_{\boldsymbol{k}n} &= s_z\sigma_z, \\
V_{\boldsymbol{k}n}^{\dagger}(\mathbb{1} \otimes \sigma_x)V_{\boldsymbol{k}n} &= s_x\sigma_x + \delta_{xz}\sigma_z,
\end{aligned} \tag{28}$$

where $s_z, s_x, \delta_{xz} \in \mathbb{R}$. This is the closest one can make the pseudospins look like spins. In general δ_{xz} is not zero, nor are the δ_{yx}, δ_{yz} from $V_{\boldsymbol{k}n}^{\dagger}(\mathbb{1} \otimes \sigma_y)V_{\boldsymbol{k}n} = s_y\sigma_y + \delta_{yx}\sigma_x + \delta_{yz}\sigma_z$. However, in SRO the only regions where $\delta_{xz}, \delta_{yx}, \delta_{yz}$ are substantially different from zero is at the nesting of the α, β, and γ bands at $k_1 = \pm k_2$ (Fig. 1). The explanation for this is the fact that spin-orbit coupling most strongly affects the band structure there.

Using the tight-binding model of SRO (Appendix B), we have explored the orientation of the $\boldsymbol{d}_{\boldsymbol{k}n}$-vectors on the α, β, and γ Fermi sheets. Everywhere except near the $k_1 = \pm k_2$ nesting of the sheets, we find that symmetric spin-orbit matrices from 1D irreps have $\boldsymbol{d}_{\boldsymbol{k}n}$ pointing along $\pm\hat{\boldsymbol{z}}$, whereas $\{\Gamma_1 \mid \Gamma_2\}$ from E_g^+ always have in-plane $\boldsymbol{d}_{\boldsymbol{k}n}$. So the nonsuppressed A_{2u} and B_{2u} from Table VI (b) have $\boldsymbol{d}_{\boldsymbol{k}n} \parallel \hat{\boldsymbol{z}}$. Moreover, among odd pairings not made of body-centered $d_a(\boldsymbol{k})$, A_{1u} and B_{1u} pairings have $\boldsymbol{d}_{\boldsymbol{k}n} \parallel \hat{\boldsymbol{z}}$ and E_u pairings have in-plane $\boldsymbol{d}_{\boldsymbol{k}n}$. Given that body-centered $\{d_1 \mid d_2\} \in E_u$ have horizontal line nodes, on the one hand, and that the spin susceptibility is intimately related to the orientation of the Balian-Werthamer $\boldsymbol{d}$-vector, on the other, this information may prove to be useful in further narrowing down the odd-pairing SC candidates.

VI. CONCLUSION

This paper was motivated by the measurements of the elastocaloric effect of Sr_2RuO_4 under strain reported in Ref. [60]. The elastocaloric effect measures, with high accuracy, the entropy derivative $\partial S(\varepsilon, T)/\partial\varepsilon$. Above T_c, the elastocaloric effect revealed a pronounced maximum in the entropy as function of strain ε. As demonstrated in Ref. [60], this maximum of $S(\varepsilon)$ can be fully accounted for by the DOS enhancement that occurs when the Fermi energy crosses the Van Hove points near the lines $(0, \pm\frac{\pi}{a}, k_3)$. Below T_c, the entropy maximum was found to transform into a minimum. This is only possible if the states near the saddle points of the electronic dispersion open a gap as one enters the SC state. Hence, with rather minimal modeling, it is possible to obtain information about the momentum-space structure of the SC gap from a thermodynamic measurement.

In order to draw more detailed conclusions about the allowed pairing states, we performed a symmetry analysis for a three-dimensional, three-band description of SRO. Here we

focus primarily on even-parity states, given the strong evidence for even parity in NMR measurements [33–35]. From a simple two-dimensional perspective, one would conclude that the SC state must open a gap at the Van Hove points $(\pm\frac{\pi}{a}, 0)$ and $(0, \pm\frac{\pi}{a})$. However, to distinguish the relevant pairing states, in particular those of the 2D irreducible representation E_g that transform like $\{d_{xz}|d_{yz}\}$, we must include the third momentum direction. It is well known that the energy dispersion of SRO is strongly anisotropic. Indeed, our analysis shows that the energy scale below which the three-dimensionality of the Fermi surface becomes important is about one kelvin, fully consistent with magneto-oscillation experiments [2]. We also show that the saddle points deviate by very small amounts $\delta k_{\text{VH,2}} \ll \frac{2\pi}{a}$ from the lines $(\pm\frac{\pi}{a}, 0, k_3)$ and $(0, \pm\frac{\pi}{a}, k_3)$. However, this need not be the case for the SC state. While the single particle spectrum of SRO is highly anisotropic, it is possible that many-body interactions that are responsible for the SC pairing couple different layers more efficiently. Hence, at least in principle, one should not exclude a strong dependence of the gap function on k_3; such dependence is crucial for the $\{d_{xz}|d_{yz}\}$-wave pairing states.

With these insights, we then turned to the symmetry analysis of potential pairing states. If one assumes for a moment that the crystal structure of SRO is simple tetragonal, one is left with only two possible even pairing states, namely, the s-wave state of A_{1g} symmetry and the $d_{x^2-y^2}$-wave state of B_{1g} symmetry. Given that fine-tuning is required for s-wave pairing to be consistent with the pair-breaking role of impurities [26–29], $d_{x^2-y^2}$-wave pairing would then appear to be the only natural pairing candidate. However, Sr_2RuO_4 is a body-centered tetragonal compound. The corresponding symmetry analysis now allows, in addition to $d_{x^2-y^2}$-wave pairing, for a $\{d_{xz} \mid d_{yz}\}$-wave state of E_g symmetry like the one given in Eq. (25).

Our analysis does, however, allow us to exclude d_{xy}-wave pairing states that transform like B_{2g} and $g_{xy(x^2-y^2)}$-wave pairing states that transform like A_{2g} as sole pairing states. Such states may at best be subleading contenders that could be added to the pairing wave function at fine-tuned points of accidental degeneracy. In addition, we can exclude $\{d_{xz} \mid d_{yz}\}$-wave pairing that is exclusively of the type given in Eq. (26). The nature of our argument does not allow us to more precisely quantify how large these subleading d_{xy}-wave or $g_{xy(x^2-y^2)}$-wave contributions are because they vanish precisely where the elastocaloric experiment is most sensitive: at the Van Hove lines. Thus, while the elastocaloric measurements do not allow for a unique determination of the superconducting order parameter symmetry, they do constrain the available options. To finally resolve the nature of superconductivity in Sr_2RuO_4 requires a better understanding of the origin of time-reversal symmetry breaking and of the orientation of line nodes.

ACKNOWLEDGMENTS

APPENDIX A: GELL-MANN MATRICES

We use the following unconventional choice for the nine Gell-Mann matrices:

$$\Lambda_0 = \begin{pmatrix} 1 & 0 & 0 \\ 0 & 1 & 0 \\ 0 & 0 & 0 \end{pmatrix}, \quad \Lambda_1 = \begin{pmatrix} 0 & 1 & 0 \\ 1 & 0 & 0 \\ 0 & 0 & 0 \end{pmatrix}, \quad \text{(A1)}$$

$$\Lambda_2 = \begin{pmatrix} 0 & -i & 0 \\ i & 0 & 0 \\ 0 & 0 & 0 \end{pmatrix}, \quad \Lambda_3 = \begin{pmatrix} 1 & 0 & 0 \\ 0 & -1 & 0 \\ 0 & 0 & 0 \end{pmatrix}, \quad \text{(A2)}$$

$$\Lambda_4 = \begin{pmatrix} 0 & 0 & 0 \\ 0 & 0 & 0 \\ 0 & 0 & \sqrt{2} \end{pmatrix}, \quad \text{(A3)}$$

$$\Lambda_5 = \begin{pmatrix} 0 & 0 & 1 \\ 0 & 0 & 0 \\ 1 & 0 & 0 \end{pmatrix}, \quad \Lambda_6 = \begin{pmatrix} 0 & 0 & -i \\ 0 & 0 & 0 \\ i & 0 & 0 \end{pmatrix}, \quad \text{(A4)}$$

$$\Lambda_7 = \begin{pmatrix} 0 & 0 & 0 \\ 0 & 0 & 1 \\ 0 & 1 & 0 \end{pmatrix}, \quad \Lambda_8 = \begin{pmatrix} 0 & 0 & 0 \\ 0 & 0 & -i \\ 0 & i & 0 \end{pmatrix}. \quad \text{(A5)}$$

They are normalized so that $\operatorname{tr}\Lambda_\mu\Lambda_\nu = 2\delta_{\mu\nu}$.

APPENDIX B: TIGHT-BINDING MODEL OF SRO

Within the effective tight-binding model of SRO based on the t_{2g} orbitals of Ru, the point group operation $g \in D_{4h}$ acts on electrons according to:

$$\hat{\mathcal{U}}^\dagger(g)\psi_{\boldsymbol{k}}\hat{\mathcal{U}}(g) = M(g) \otimes S(g)\psi_{R(g^{-1})\boldsymbol{k}}, \quad \text{(B1)}$$

where $\psi_{\boldsymbol{k}}$ are column vectors of fermionic destruction operators in the basis $(d_{yz\uparrow}, d_{yz\downarrow}, d_{zx\uparrow}, d_{zx\downarrow}, d_{xy\uparrow}, d_{xy\downarrow})^\mathsf{T}$, $\hat{\mathcal{U}}(g)$ are the Fock-space symmetry operators, and R, M, S are unitary representations of D_{4h} whose generators are listed in Table VII. Time-reversal Θ acts like

$$\Theta^{-1}\psi_{\boldsymbol{k}}\Theta = (\mathbb{1} \otimes i\sigma_y)\psi_{-\boldsymbol{k}}, \quad \text{(B2)}$$

where $\mathbb{1}$ is the 3×3 identity matrix and σ_μ are the Pauli matrices.

Since there is only one ruthenium atom per a body-centered unit cell, the tight-binding Hamiltonian takes the form

$$H_0 = -\sum_{\boldsymbol{R},\boldsymbol{\delta}} \psi_{\boldsymbol{R}+\boldsymbol{\delta}}^\dagger \left[T_{\boldsymbol{\delta}} \otimes \mathbb{1} + i\sum_{\mu=1}^3 \Lambda_{\boldsymbol{\delta};\mu} \otimes \sigma_\mu \right] \psi_{\boldsymbol{R}}, \quad \text{(B3)}$$

where $\boldsymbol{R}, \boldsymbol{\delta}$ go over the body-centered tetragonal lattice whose primitive lattice vectors are

$$\boldsymbol{a}_1 = a\hat{\boldsymbol{e}}_1, \quad \boldsymbol{a}_2 = a\hat{\boldsymbol{e}}_2, \quad \boldsymbol{a}_3 = \tfrac{1}{2}(a\hat{\boldsymbol{e}}_1 + a\hat{\boldsymbol{e}}_2 + c\hat{\boldsymbol{e}}_3). \quad \text{(B4)}$$

The Hamiltonian is hermitian only when $T_{-\boldsymbol{\delta}} = T_{\boldsymbol{\delta}}^\dagger$ and $\Lambda_{-\boldsymbol{\delta};\mu} = -\Lambda_{\boldsymbol{\delta};\mu}^\dagger$. Point group symmetries constrain and relate different hopping amplitudes:

$$M^\dagger(g)T_{\boldsymbol{\delta}}M(g) = T_{R(g^{-1})\boldsymbol{\delta}}, \quad \text{(B5)}$$

$$M^\dagger(g)\Lambda_{\boldsymbol{\delta};\mu}M(g) = \det R(g) \sum_{\nu=1}^3 R_{\mu\nu}(g)\Lambda_{R(g^{-1})\boldsymbol{\delta};\nu}. \quad \text{(B6)}$$

To ensure time-reversal invariance, all matrix elements must be made real, i.e., $T_{\boldsymbol{\delta}}^* = T_{\boldsymbol{\delta}}$ and $\Lambda_{\boldsymbol{\delta};\mu}^* = \Lambda_{\boldsymbol{\delta};\mu}$.

Symmetries that map $\boldsymbol{\delta}$ to itself constrain the forms of the hopping amplitudes. For the eight closest $\boldsymbol{\delta}$ of SRO, we find that

$$T_{\boldsymbol{0}} = \begin{pmatrix} \mu_{1D} & 0 & 0 \\ 0 & \mu_{1D} & 0 \\ 0 & 0 & \mu_{2D} \end{pmatrix}, \quad T_{\boldsymbol{a}_1} = \begin{pmatrix} t_1 & 0 & 0 \\ 0 & t_2 & 0 \\ 0 & 0 & \bar{t}_1 \end{pmatrix}, \quad \text{(B7)}$$

$$T_{\boldsymbol{a}_1+\boldsymbol{a}_2} = \begin{pmatrix} t_3 & t_{i1} & 0 \\ t_{i1} & t_3 & 0 \\ 0 & 0 & \bar{t}_2 \end{pmatrix}, \quad T_{\boldsymbol{a}_3} = \begin{pmatrix} t_4 & t_{i2} & t_j \\ t_{i2} & t_4 & t_j \\ t_j & t_j & \bar{t}_3 \end{pmatrix}, \quad \text{(B8)}$$

$$T_{2\boldsymbol{a}_1} = \begin{pmatrix} t_5 & 0 & 0 \\ 0 & t_6 & 0 \\ 0 & 0 & \bar{t}_4 \end{pmatrix}, \quad T_{2\boldsymbol{a}_1+\boldsymbol{a}_2} = \begin{pmatrix} t_7 & t_{i3} & 0 \\ t_{i3} & t_8 & 0 \\ 0 & 0 & \bar{t}_5 \end{pmatrix}, \quad \text{(B9)}$$

$$T_{2(\boldsymbol{a}_1+\boldsymbol{a}_2)} = \begin{pmatrix} t_9 & t_{i4} & 0 \\ t_{i4} & t_9 & 0 \\ 0 & 0 & \bar{t}_6 \end{pmatrix}, \quad T_{3\boldsymbol{a}_1} = \begin{pmatrix} t_{10} & 0 & 0 \\ 0 & t_{11} & 0 \\ 0 & 0 & \bar{t}_7 \end{pmatrix}. \quad \text{(B10)}$$

Among these closest and thus largest $T_{\boldsymbol{\delta}}$, only $T_{\boldsymbol{a}_3}$ connects different layers, reflecting the high anisotropy of SRO. Moreover, it is only through $T_{\boldsymbol{a}_3}$ that the body-centered periodicity

TABLE VII. The generators of the representations R, M, and S of the point group D_{4h}. C_{4z} is a rotation by $\pi/2$ around z. C'_{2x} and C''_{2d} are rotations by π around x and the diagonal $x + y$, respectively. P is parity.

g	$R(g)$	$M(g)$	$S(g)$
C_{4z}	$\begin{pmatrix} 0 & -1 & 0 \\ 1 & 0 & 0 \\ 0 & 0 & 1 \end{pmatrix}$	$\begin{pmatrix} 0 & 1 & 0 \\ -1 & 0 & 0 \\ 0 & 0 & -1 \end{pmatrix}$	$\frac{\sigma_0 - i\sigma_z}{\sqrt{2}}$
C'_{2x}	$\begin{pmatrix} 1 & 0 & 0 \\ 0 & -1 & 0 \\ 0 & 0 & -1 \end{pmatrix}$	$\begin{pmatrix} 1 & 0 & 0 \\ 0 & -1 & 0 \\ 0 & 0 & -1 \end{pmatrix}$	$-i\sigma_x$
C''_{2d}	$\begin{pmatrix} 0 & 1 & 0 \\ 1 & 0 & 0 \\ 0 & 0 & -1 \end{pmatrix}$	$\begin{pmatrix} 0 & -1 & 0 \\ -1 & 0 & 0 \\ 0 & 0 & 1 \end{pmatrix}$	$-i\frac{\sigma_x + \sigma_y}{\sqrt{2}}$
P	$-\mathbb{1}$	$\mathbb{1}$	σ_0

TABLE VIII. The values of our tight-binding model parameters in meV.

(a) The parameter values according to Ref. [109].
The parameters set to zero have not been considered in Ref. [109].

t_1	t_2	t_3	t_4	t_5	t_6	t_7	t_8	t_9
27.8	257.8	−22.4	13.6	3.2	−35.5	0	−4.7	0

t_{10}	t_{11}	$\bar{t}_1$	$\bar{t}_2$	$\bar{t}_3$	$\bar{t}_4$	$\bar{t}_5$	$\bar{t}_6$	$\bar{t}_7$
0	−2.4	356.8	126.3	−1.0	17.0	22.3	0	0

μ_{1D}	μ_{2D}	t_{i1}	t_{i2}	t_{i3}	t_{i4}	t_j	η_1	η_2
286.9	351.9	−2.0	7.8	0	0	2.7	59.2	59.2

(b) The parameters according to other references.
Those parameters not listed vanish.

t_1	t_2	$\bar{t}_1$	$\bar{t}_2$	$\bar{t}_4$	μ_{1D}	μ_{2D}	t_{i1}	η_1	η_2	Ref.
16	145	81	39	5	122	122	0	32	32	[113]
9	88	80	40	5	109	109	0	35	35	[114]
13	165	119	49	0	178	176	21	0	0	[123]

TABLE IX. A sample of possible pairing wave functions $d_a(\boldsymbol{k})$ categorized according to the transformation rule (C5). The irrep subscripts g and u mean even and odd under parity, respectively. The two-component $\{d_1(\boldsymbol{k}) \mid d_2(\boldsymbol{k})\}$ transform according to the $\rho^{(E)}(g)$ given in Eq. (C4). $\boldsymbol{k} = (k_1, k_2, k_3)$ and $\kappa_1 = ak_1$, $\kappa_2 = ak_2$, $\kappa_3 = ck_3$. Highlighted red are those wave functions that are periodic under body-centered translations, but not under simple tetragonal translations.

A_{1g}	$1, \cos\kappa_1 + \cos\kappa_2, \cos\kappa_3, \cos\kappa_1 \cos\kappa_2$
A_{2g}	$(\cos\kappa_1 - \cos\kappa_2)\sin\kappa_1 \sin\kappa_2$
B_{1g}	$\cos\kappa_1 - \cos\kappa_2$
B_{2g}	$\sin\kappa_1 \sin\kappa_2, \sin\frac{1}{2}\kappa_1 \sin\frac{1}{2}\kappa_2 \cos\frac{1}{2}\kappa_3$
E_g	$\{\sin\kappa_2 \sin\kappa_3 \mid -\sin\kappa_1 \sin\kappa_3\},$ $\{\cos\frac{1}{2}\kappa_1 \sin\frac{1}{2}\kappa_2 \sin\frac{1}{2}\kappa_3 \mid -\sin\frac{1}{2}\kappa_1 \cos\frac{1}{2}\kappa_2 \sin\frac{1}{2}\kappa_3\}$
A_{1u}	$(\cos\kappa_1 - \cos\kappa_2)\sin\frac{1}{2}\kappa_1 \sin\frac{1}{2}\kappa_2 \sin\frac{1}{2}\kappa_3$
A_{2u}	$\sin\kappa_3, \cos\frac{1}{2}\kappa_1 \cos\frac{1}{2}\kappa_2 \sin\frac{1}{2}\kappa_3$
B_{1u}	$\sin\frac{1}{2}\kappa_1 \sin\frac{1}{2}\kappa_2 \sin\frac{1}{2}\kappa_3$
B_{2u}	$(\cos\kappa_1 - \cos\kappa_2)\sin\kappa_3$
E_u	$\{\sin\kappa_1 \mid \sin\kappa_2\},$ $\{(\cos\kappa_1 - \cos\kappa_2)\sin\kappa_1 \mid -(\cos\kappa_1 - \cos\kappa_2)\sin\kappa_2\},$ $\{\sin\frac{1}{2}\kappa_1 \cos\frac{1}{2}\kappa_2 \cos\frac{1}{2}\kappa_3 \mid \cos\frac{1}{2}\kappa_1 \sin\frac{1}{2}\kappa_2 \cos\frac{1}{2}\kappa_3\}$

of SRO is felt on the level of the one-particle Hamiltonian. The on-site spin-orbit coupling takes the form

$$\Lambda_{\mathbf{0};1} = \begin{pmatrix} 0 & 0 & 0 \\ 0 & 0 & -\eta_1 \\ 0 & \eta_1 & 0 \end{pmatrix}, \quad \Lambda_{\mathbf{0};2} = \begin{pmatrix} 0 & 0 & \eta_1 \\ 0 & 0 & 0 \\ -\eta_1 & 0 & 0 \end{pmatrix},$$

(B11)

$$\Lambda_{\mathbf{0};3} = \begin{pmatrix} 0 & -\eta_2 & 0 \\ \eta_2 & 0 & 0 \\ 0 & 0 & 0 \end{pmatrix}.$$

(B12)

Off-site ($\boldsymbol{k}$-dependent) spin-orbit coupling we shall not include, although one should keep in mind that some [16] have found that it has a large effect on the preferred Cooper pairing, even when small.

For our analysis, we have used the tight-binding parameter values of Ref. [110], which they found by fitting to the ARPES-based tight-binding 17-band model of Ref. [124]. Their tight-binding parameter values are reproduced in Table VIII. The hopping amplitudes of Refs. [16,110] are broadly in agreement, as one would expect given that both were fitted to Ref. [124]. However, the hoppings of both [16,110] are by a factor of two or so larger than those of Refs. [113,114,123], which are also ARPES-derived; see Table VIII. Although all these models give the correct shapes for the Fermi sheets, find that the γ band is responsible for over 50 % of the normal-state DOS, and predict a roughly 20 % increase in the DOS at Van Hove strain, consistent with our entropy data (Fig. 2), the predicted values for the total DOS differ by a factor of two. Only Ref. [113] has checked that their model gives a total DOS ($g \approx 17$ states per eV per body-centered tetragonal unit cell) that is consistent with the experimentally measured Sommerfeld coefficient $\gamma = (\pi^2/3)Rg \approx 40$ mJ/(K^2 mol) [82–84], where R is the molar gas constant. The main takeaway is that the various

estimates cited in the main text might be off by a factor of two, which is still sufficient for our purposes and does not impact our argument in any way.

TABLE X. Spin-orbit matrices Γ_a categorized according to the transformation rule (C6) and (anti)symmetry (C7). The irrep subscript g means even under parity. The irrep superscripts $\pm$ are the values of s [Eq. (C7)], so $+$ $(-)$ means that the matrices are (anti)symmetric under transposition. The matrices are written in terms of $[\mu, \nu] \equiv \Lambda_\mu \otimes \sigma_\nu(i\sigma_y)$, where the Gell-Mann matrices Λ_μ have been listed in Appendix A. Subtractions of pairs $[\mu, \nu]$ represent subtractions of the respective matrices. The two-component $\{\Gamma_1 \mid \Gamma_2\}$ transform according to the $\rho^{(E)}(g)$ given in Eq. (C4). Highlighted blue are the singlet and triplet pairings with trivial orbital structures, typical of one-band SC.

A_{1g}^-	$[0, 0], [2, z], [4, 0], [6, y] - [8, x]$
A_{2g}^-	$[6, x] + [8, y]$
B_{1g}^-	$[3, 0], [6, y] + [8, x]$
B_{2g}^-	$[1, 0], [6, x] - [8, y]$
E_g^-	$\{[2, y] \mid -[2, x]\}, \{[7, 0] \mid -[5, 0]\}, \{[6, z] \mid [8, z]\}$
A_{1g}^+	$[5, y] - [7, x]$
A_{2g}^+	$[0, z], [2, 0], [4, z], [5, x] + [7, y]$
B_{1g}^+	$[1, z], [5, y] + [7, x]$
B_{2g}^+	$[3, z], [5, x] - [7, y]$
E_g^+	$\{[0, x] \mid [0, y]\}, \{[1, y] \mid [1, x]\}, \{[3, x] \mid -[3, y]\},$ $\{[4, x] \mid [4, y]\}, \{[5, z] \mid [7, z]\}, \{[8, 0] \mid -[6, 0]\}$

In momentum space, the tight-binding Hamiltonian equals

$$H_{\boldsymbol{k}} = -\sum_{\boldsymbol{\delta}} \left[T_{\boldsymbol{\delta}} \otimes \mathbb{1} + \mathrm{i} \sum_{\mu=1}^{3} \Lambda_{\boldsymbol{\delta};\mu} \otimes \sigma_{\mu} \right] e^{-\mathrm{i}\boldsymbol{k}\cdot\boldsymbol{\delta}} \tag{B13}$$

$$= \begin{pmatrix} \epsilon_{1\mathrm{D}}(\boldsymbol{k}) & \epsilon_i(\boldsymbol{k}) & \epsilon_j(\boldsymbol{k}) \\ \epsilon_i(\boldsymbol{k}) & \tilde{\epsilon}_{1\mathrm{D}}(\boldsymbol{k}) & \tilde{\epsilon}_j(\boldsymbol{k}) \\ \epsilon_j(\boldsymbol{k}) & \tilde{\epsilon}_j(\boldsymbol{k}) & \epsilon_{2\mathrm{D}}(\boldsymbol{k}) \end{pmatrix} \otimes \sigma_0 + \begin{pmatrix} 0 & \mathrm{i}\eta_2\sigma_3 & -\mathrm{i}\eta_1\sigma_2 \\ -\mathrm{i}\eta_2\sigma_3 & 0 & \mathrm{i}\eta_1\sigma_1 \\ \mathrm{i}\eta_1\sigma_2 & -\mathrm{i}\eta_1\sigma_1 & 0 \end{pmatrix}, \tag{B14}$$

where $\tilde{\epsilon}_{1\mathrm{D}}(k_1, k_2, k_3) = \epsilon_{1\mathrm{D}}(k_2, k_1, k_3)$, $\tilde{\epsilon}_j(k_1, k_2, k_3) = \epsilon_j(k_2, k_1, k_3)$, and

$$\epsilon_{1\mathrm{D}}(\boldsymbol{k}) = -\mu_{1\mathrm{D}} - 2t_1 \cos\kappa_1 - 2t_2 \cos\kappa_2 - 4t_3 \cos\kappa_1 \cos\kappa_2 - 8t_4 \cos\tfrac{1}{2}\kappa_1 \cos\tfrac{1}{2}\kappa_2 \cos\tfrac{1}{2}\kappa_3 - 2t_5 \cos 2\kappa_1 - 2t_6 \cos 2\kappa_2$$
$$- 4t_7 \cos 2\kappa_1 \cos\kappa_2 - 4t_8 \cos\kappa_1 \cos 2\kappa_2 - 4t_9 \cos 2\kappa_1 \cos 2\kappa_2 - 2t_{10} \cos 3\kappa_1 - 2t_{11} \cos 3\kappa_2, \tag{B15}$$

$$\epsilon_{2\mathrm{D}}(\boldsymbol{k}) = -\mu_{2\mathrm{D}} - 2\bar{t}_1(\cos\kappa_1 + \cos\kappa_2) - 4\bar{t}_2 \cos\kappa_1 \cos\kappa_2 - 8\bar{t}_3 \cos\tfrac{1}{2}\kappa_1 \cos\tfrac{1}{2}\kappa_2 \cos\tfrac{1}{2}\kappa_3 - 2\bar{t}_4(\cos 2\kappa_1 + \cos 2\kappa_2)$$
$$- 4\bar{t}_5(\cos 2\kappa_1 \cos\kappa_2 + \cos\kappa_1 \cos 2\kappa_2) - 4\bar{t}_6 \cos 2\kappa_1 \cos 2\kappa_2 - 2\bar{t}_7(\cos 3\kappa_1 + \cos 3\kappa_2), \tag{B16}$$

$$\epsilon_i(\boldsymbol{k}) = 4t_{i1} \sin\kappa_1 \sin\kappa_2 + 8t_{i2} \sin\tfrac{1}{2}\kappa_1 \sin\tfrac{1}{2}\kappa_2 \cos\tfrac{1}{2}\kappa_3 + 8t_{i3}(\cos\kappa_1 + \cos\kappa_2) \sin\kappa_1 \sin\kappa_2 + 4t_{i4} \sin 2\kappa_1 \sin 2\kappa_2, \tag{B17}$$

$$\epsilon_j(\boldsymbol{k}) = 8t_j \sin\tfrac{1}{2}\kappa_1 \cos\tfrac{1}{2}\kappa_2 \sin\tfrac{1}{2}\kappa_3. \tag{B18}$$

Above $\boldsymbol{k} = (k_1, k_2, k_3)$, $\kappa_1 = ak_1$, $\kappa_2 = ak_2$, and $\kappa_3 = ck_3$.

The coupling to strain, needed for Fig. 1, was taken from the Supplementary information of Ref. [60]. The dispersion of the γ band near the Van Hove line $(0, \frac{\pi}{a}, k_3)$, provided in the main text in Eqs. (9) and (18), was found by diagonalizing $H_{\boldsymbol{k}}$ with the parameter values of Ref. [110].

APPENDIX C: SUPERCONDUCTING STATES OF SRO

For the purpose of classifying even-frequency pairings, it is sufficient to consider the static case because the two behave the same symmetry-wise [125]. Odd-frequency pairings are beyond the scope of this article. On the mean-field level, static zero-momentum SC is described by a pairing term in the Hamiltonian of the form:

$$H_{\mathrm{SC}} = \sum_{\boldsymbol{k}\alpha\beta} \psi_{\boldsymbol{k}\alpha}^{\dagger} \Delta_{\alpha\beta}(\boldsymbol{k}) \psi_{-\boldsymbol{k}\beta}^{\dagger} + \mathrm{H.c.}, \tag{C1}$$

where α, β are spin-orbit indices. Because of the fermionic anticommutation, the SC gap matrix $\Delta_{\alpha\beta}(\boldsymbol{k})$ satisfies the exchange property:

$$\Delta^{\mathsf{T}}(\boldsymbol{k}) = -\Delta(-\boldsymbol{k}), \tag{C2}$$

where T is transposition.

If the pairing were conventional, all point group operations would be preserved and $\hat{\mathcal{U}}^{\dagger}(g)H_{\mathrm{SC}}\hat{\mathcal{U}}(g) = H_{\mathrm{SC}}$ would hold for all $g \in D_{4h}$, giving the constraint $U^{\dagger}(g)\Delta(R(g)\boldsymbol{k})U^*(g) = \Delta(\boldsymbol{k})$, where $U(g) \equiv M(g) \otimes S(g)$. Unconventional pairing is classified by the way it breaks this constraint:

$$U^{\dagger}(g)\Delta_d(R(g)\boldsymbol{k})U^*(g) = \sum_{b=1}^{\dim\lambda} \rho_{ab}^{(\lambda)}(g)\Delta_b(\boldsymbol{k}). \tag{C3}$$

Here, λ is an irrep of D_{4h}, a, b are indices internal to the irrep, and $\rho_{ab}^{(\lambda)}$ are the corresponding matrices. Only for the 2D irreps $E_{g/u}$ are there multiple possible $\rho_{ab}^{(\lambda)}$. We choose (cf. representation R):

$$\rho^{(E)}(C_{4z}) = \begin{pmatrix} 0 & -1 \\ 1 & 0 \end{pmatrix}, \quad \rho^{(E)}(C_{2x}') = \begin{pmatrix} 1 & 0 \\ 0 & -1 \end{pmatrix},$$

$$\rho^{(E)}(C_{2d}'') = \begin{pmatrix} 0 & 1 \\ 1 & 0 \end{pmatrix}, \quad \rho^{(E_{g/u})}(P) = \pm\begin{pmatrix} 1 & 0 \\ 0 & 1 \end{pmatrix}. \tag{C4}$$

To construct a $\Delta_a(\boldsymbol{k})$ that properly transforms according to Eq. (C3), we need to combine the momentum dependence and spin-orbit structure in just the right way. This is accomplished [106–108] by first separately classifying pairing wave

TABLE XI. Direct sum decompositions of the direct products between irreps of D_{4h}. Since all Γ irreps are even, the parity of the d irrep and direct product irrep are the same so we have suppressed their g/u subscripts. All E irreps transform according to the same 2D representation (C4).

$\otimes$	$A_1\{d\}$	$A_2\{d\}$	$B_1\{d\}$	$B_2\{d\}$	$E\{d_1 \mid d_2\}$
$A_{1g}\{\Gamma\}$	$A_1\{\Gamma d\}$	$A_2\{\Gamma d\}$	$B_1\{\Gamma d\}$	$B_2\{\Gamma d\}$	$E\{\Gamma d_1 \mid \Gamma d_2\}$
$A_{2g}\{\Gamma\}$	$A_2\{\Gamma d\}$	$A_1\{\Gamma d\}$	$B_2\{\Gamma d\}$	$B_1\{\Gamma d\}$	$E\{\Gamma d_2 \mid -\Gamma d_1\}$
$B_{1g}\{\Gamma\}$	$B_1\{\Gamma d\}$	$B_2\{\Gamma d\}$	$A_1\{\Gamma d\}$	$A_2\{\Gamma d\}$	$E\{\Gamma d_1 \mid -\Gamma d_2\}$
$B_{2g}\{\Gamma\}$	$B_2\{\Gamma d\}$	$B_1\{\Gamma d\}$	$A_2\{\Gamma d\}$	$A_1\{\Gamma d\}$	$E\{\Gamma d_2 \mid \Gamma d_1\}$
$E_g\begin{Bmatrix}\Gamma_1\\\Gamma_2\end{Bmatrix}$	$E\begin{Bmatrix}\Gamma_1 d\\\Gamma_2 d\end{Bmatrix}$	$E\begin{Bmatrix}\Gamma_2 d\\-\Gamma_1 d\end{Bmatrix}$	$E\begin{Bmatrix}\Gamma_1 d\\-\Gamma_2 d\end{Bmatrix}$	$E\begin{Bmatrix}\Gamma_2 d\\\Gamma_1 d\end{Bmatrix}$	$A_1\{\Gamma_1 d_1 + \Gamma_2 d_2\} \oplus A_2\{\Gamma_1 d_2 - \Gamma_2 d_1\}$ $\oplus B_1\{\Gamma_1 d_1 - \Gamma_2 d_2\} \oplus B_2\{\Gamma_1 d_2 + \Gamma_2 d_1\}$

functions and spin-orbit matrices (Tables IX and X), and then combining them according to a set of rules (Table XI). Let us emphasize that the emergent SC order parameter that enters Ginzburg-Landau theory belongs to the irrep determined by the total SC gap $\Delta_a(\mathbf{k})$ according to Eq. (C3), and not to the irreps of its momentum or spin-orbit parts.

Pairing wave functions $d_a(\mathbf{k})$ are classified according to

$$d_a(R(g)\mathbf{k}) = \sum_{b=1}^{\dim\lambda} \rho_{ab}^{(\lambda)}(g)d_b(\mathbf{k}). \tag{C5}$$

All $d_a(\mathbf{k})$ should be made periodic, just like $\Delta_a(\mathbf{k})$. If we call $\kappa_1 = ak_1$, $\kappa_2 = ak_2$, and $\kappa_3 = ck_3$, the primitive translations of a body-centered tetragonal lattice map $(\kappa_1, \kappa_2, \kappa_3)$ to $(\kappa_1 + 2\pi, \kappa_2, \kappa_3 - 2\pi)$, $(\kappa_1, \kappa_2 + 2\pi, \kappa_3 - 2\pi)$, and $(\kappa_1, \kappa_2, \kappa_3 + 4\pi)$. Conventionally, we also make $d_a(\mathbf{k})$ real so that TRSB is seen through imaginary coefficients preceding $d_a(\mathbf{k})$. Examples of pairing wave functions are provided in Table IX.

When it comes to spin-orbit matrices Γ_a, notice that $U(P) = \mathbb{1}$ leaves the matrix part of Eq. (C3) invariant. This means that all spin-orbit matrices are even.[6] We classify them according to

$$U^\dagger(g)\Gamma_a U^*(g) = \sum_{b=1}^{\dim\lambda} \rho_{ab}^{(\lambda)}(g)\Gamma_b, \tag{C6}$$

where $U(g) = M(g) \otimes S(g)$. Given the transposition in Eq. (C2), it is natural to further categorize Γ_a according to (anti)symmetry:

$$\Gamma_a^\mathsf{T} = s\Gamma_a, \tag{C7}$$

where $s \in \{\pm 1\}$. We shall also ensure time-reversal invariance:

$$(\mathbb{1} \otimes i\sigma_y)\Gamma_a^*(\mathbb{1} \otimes i\sigma_y) = \Gamma_a^\mathsf{T}, \tag{C8}$$

so that TRSB manifests itself through imaginary prefactors. As the basis of the orbital part of Γ_a, we use Gell-Mann matrices Λ_μ (Appendix A). The spin-orbit matrices we write in terms of these:

$$\Gamma_a \sim \sum \Lambda_\mu \otimes \sigma_\nu(i\sigma_y). \tag{C9}$$

Given that $\Lambda_\mu^\dagger = \Lambda_\mu$, written thusly Γ_a automatically satisfy time-reversal invariance (C8). In three-band systems, there are in total $4 \cdot 3^2 = 36$ possible Γ_a, of which 15 are antisymmetric and 21 are symmetric. The categorization of all $\Lambda_\mu \otimes \sigma_\nu(i\sigma_y) \equiv [\mu, \nu]$ is given in Table X.

SC gap matrices $\Delta(\mathbf{k})$ are constructed by combining pairing wave functions $d_a(\mathbf{k})$ and spin-orbit matrices Γ_a. Because of the exchange property (C2), we may only combine even $d_a(\mathbf{k})$ with antisymmetric Γ_a, or odd $d_a(\mathbf{k})$ with symmetric Γ_a. Now consider a $\{d_a(\mathbf{k})\} \in \lambda_d$ and $\{\Gamma_a\} \in \lambda_\Gamma$, where λ_d and λ_Γ are irreps. The object $\Delta_{ab}(\mathbf{k}) \equiv \Gamma_a d_b(\mathbf{k})$ then transforms

---

[6]Odd spin-orbit matrices occur when the conduction bands mix parities, as happens, for example, for topological band structures.

(a) $\Delta_{\mathbf{k}} = \Lambda_0(i\sigma_y)$

(b) $\Delta_{\mathbf{k}} = \Lambda_2\sigma_3(i\sigma_y)$

(c) $\Delta_{\mathbf{k}} = \Lambda_4(i\sigma_y)$

(d) $\Delta_{\mathbf{k}} = (\Lambda_6\sigma_y - \Lambda_8\sigma_x)(i\sigma_y)$

(e) $\Delta_{\mathbf{k}} = \Lambda_3(i\sigma_y)(\cos\kappa_1 - \cos\kappa_2)$

(f) $\Delta_{\mathbf{k}} = (\Lambda_6\sigma_y + \Lambda_8\sigma_x)(i\sigma_y)(\cos\kappa_1 - \cos\kappa_2)$
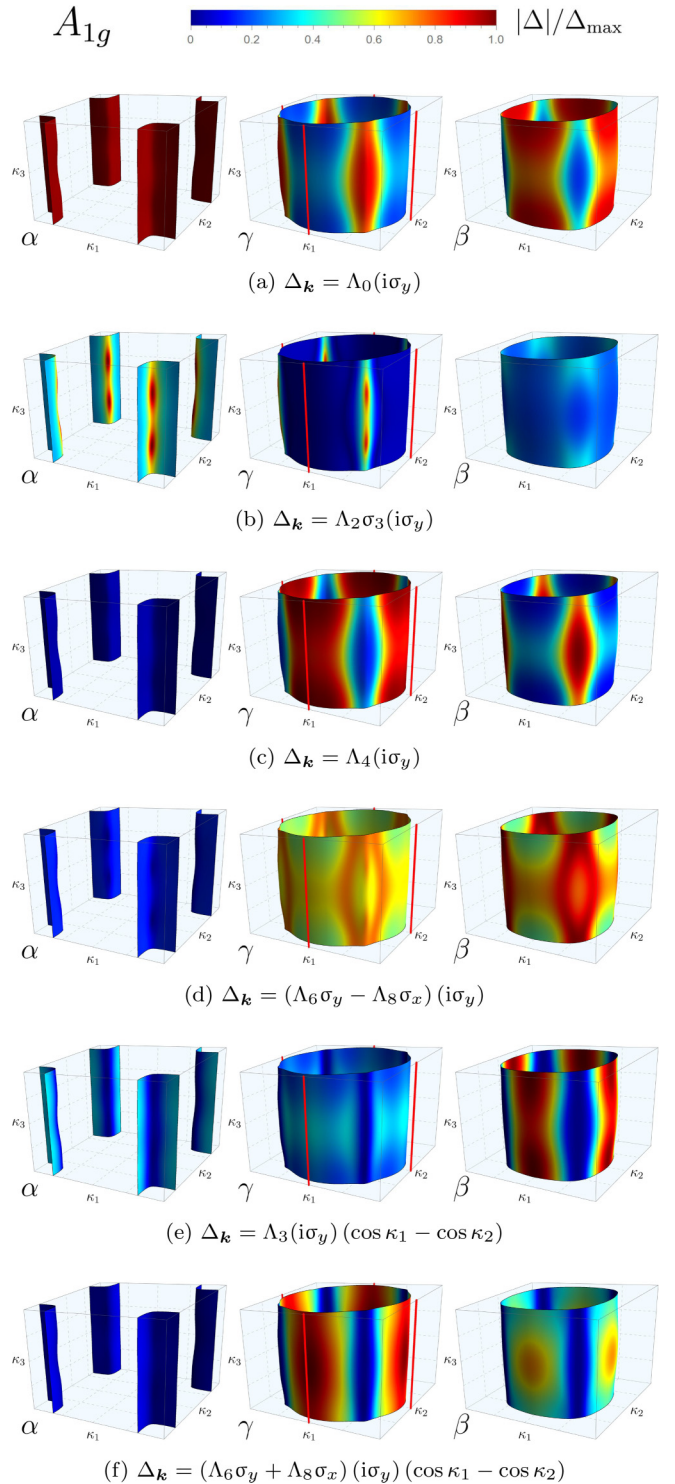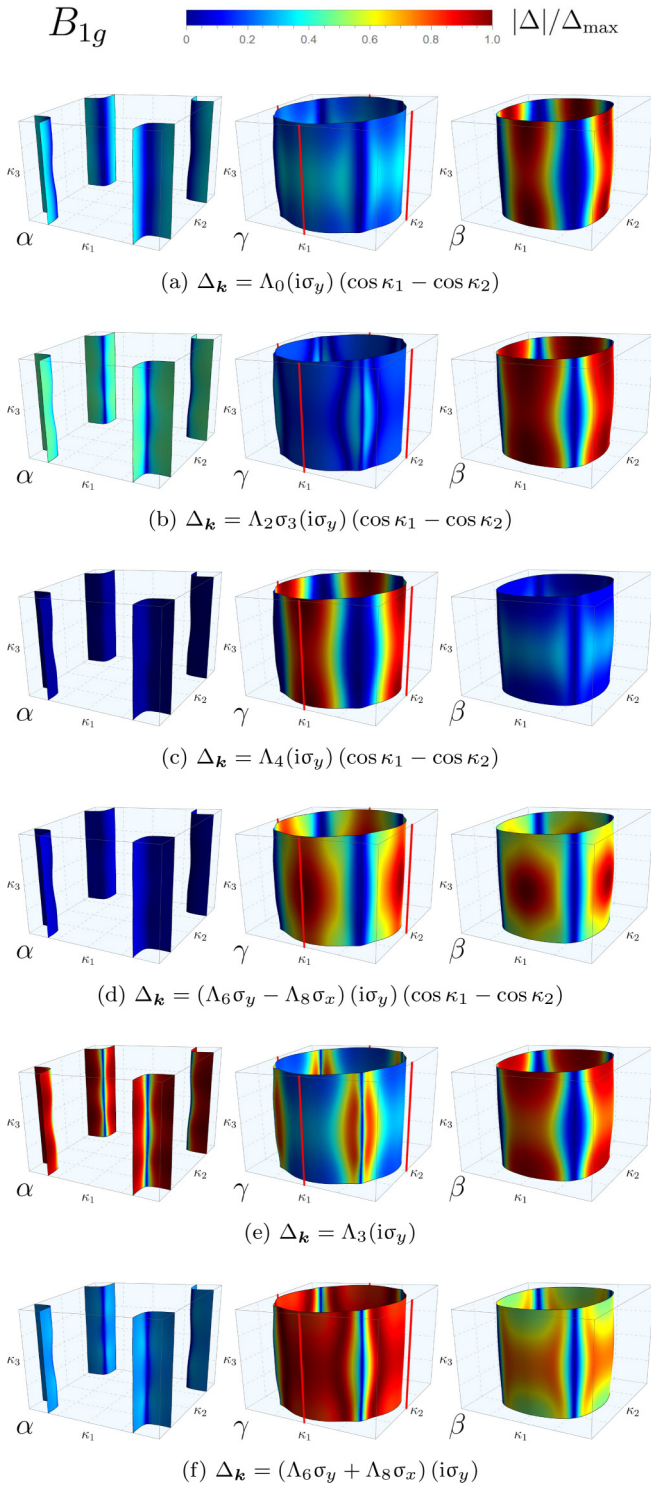
FIG. 6. Projections onto the Fermi sheets of a number of Van Hove line-gapping SC states $\Delta_{\mathbf{k}}$ belonging to the A_{1g} irrep. See the text for details.

according to the $\lambda_\Gamma \otimes \lambda_d$ representation:

$$U^\dagger(g)\Delta_{ab}(R(g)\mathbf{k})U^*(g)$$
$$= \sum_{a'=1}^{\dim\lambda_\Gamma}\sum_{b'=1}^{\dim\lambda_d} \rho_{aa'}^{(\lambda_\Gamma)}(g)\rho_{bb'}^{(\lambda_d)}(g)\Delta_{a'b'}(\mathbf{k}). \tag{C10}$$

B_{1g}

(a) $\Delta_{\boldsymbol{k}} = \Lambda_0(\mathrm{i}\sigma_y)(\cos\kappa_1 - \cos\kappa_2)$

(b) $\Delta_{\boldsymbol{k}} = \Lambda_2\sigma_3(\mathrm{i}\sigma_y)(\cos\kappa_1 - \cos\kappa_2)$

(c) $\Delta_{\boldsymbol{k}} = \Lambda_4(\mathrm{i}\sigma_y)(\cos\kappa_1 - \cos\kappa_2)$

(d) $\Delta_{\boldsymbol{k}} = (\Lambda_6\sigma_y - \Lambda_8\sigma_x)(\mathrm{i}\sigma_y)(\cos\kappa_1 - \cos\kappa_2)$

(e) $\Delta_{\boldsymbol{k}} = \Lambda_3(\mathrm{i}\sigma_y)$

(f) $\Delta_{\boldsymbol{k}} = (\Lambda_6\sigma_y + \Lambda_8\sigma_x)(\mathrm{i}\sigma_y)$

FIG. 7. Projections onto the Fermi sheets of a number of Van Hove line-gapping SC states $\Delta_{\boldsymbol{k}}$ belonging to the B_{1g} irrep. See the text for details.

E_g

(a) $\Delta_{\boldsymbol{k}} = \Lambda_0(\mathrm{i}\sigma_y)d_{(x\pm\mathrm{i}y)z}(\boldsymbol{k})$

(b) $\Delta_{\boldsymbol{k}} = \Lambda_2\sigma_3(\mathrm{i}\sigma_y)d_{(x\pm\mathrm{i}y)z}(\boldsymbol{k})$

(c) $\Delta_{\boldsymbol{k}} = \Lambda_4(\mathrm{i}\sigma_y)d_{(x\pm\mathrm{i}y)z}(\boldsymbol{k})$

(d) $\Delta_{\boldsymbol{k}} = (\Lambda_6\sigma_y - \Lambda_8\sigma_x)(\mathrm{i}\sigma_y)d_{(x\pm\mathrm{i}y)z}(\boldsymbol{k})$

(e) $\Delta_{\boldsymbol{k}} = \Lambda_3(\mathrm{i}\sigma_y)d_{(x\pm\mathrm{i}y)z}(\boldsymbol{k})$

(f) $\Delta_{\boldsymbol{k}} = (\Lambda_6\sigma_y + \Lambda_8\sigma_x)(\mathrm{i}\sigma_y)d_{(x\pm\mathrm{i}y)z}(\boldsymbol{k})$

FIG. 8. Projections onto the Fermi sheets of a number of chiral Van Hove line-gapping SC states $\Delta_{\boldsymbol{k}}$ belonging to the E_g irrep. See the text for details.

Since we want to construct SC gap matrices that transform according to *irreducible* representations [Eq. (C3)], we decomposed $\Delta_{ab}(\boldsymbol{k})$ into irreducible parts with the help of Table XI. The most general $\{\Delta_a(\boldsymbol{k})\}$ belonging to irrep λ_Δ is then given by a sum over all possible $\{d_a(\boldsymbol{k})\} \in \lambda_d$ and $\{\Gamma_a\} \in \lambda_\Gamma$ such that $\lambda_\Delta \in \lambda_\Gamma \otimes \lambda_d$.
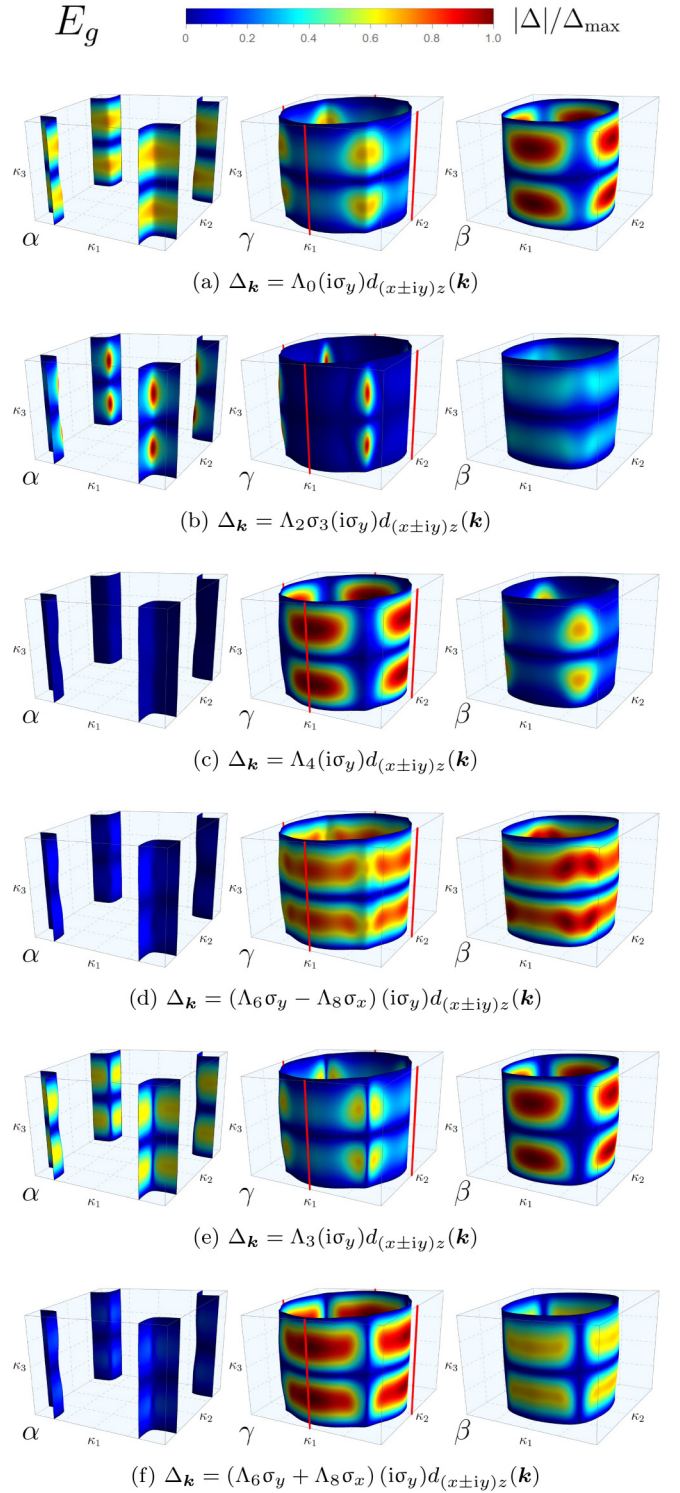
For example, let us construct SC gap matrices belonging to B_{1g}. In Table XI, every row has a B_1, meaning antisymmetric Γ_a belonging to every irrep could be used. Combining $[0, 0] = \Lambda_0(\mathrm{i}\sigma_y) \in A_{1g}^-$ and $\cos\kappa_1 - \cos\kappa_2 \in B_{1g}$ gives a $\Delta(\boldsymbol{k}) = \Lambda_0(\mathrm{i}\sigma_y)(\cos\kappa_1 - \cos\kappa_2) \in B_{1g}$, but so do

many others:

$$A_{1g}^- \otimes B_{1g}: \quad (\Lambda_6 \sigma_y - \Lambda_8 \sigma_x)(i\sigma_y)(\cos \kappa_1 - \cos \kappa_2),$$

$$A_{2g}^- \otimes B_{2g}: \quad (\Lambda_6 \sigma_x + \Lambda_8 \sigma_y)(i\sigma_y) \sin \kappa_1 \sin \kappa_2,$$

$$B_{1g}^- \otimes A_{1g}: \quad \Lambda_3(i\sigma_y) \cos \kappa_1 \cos \kappa_2,$$

$$B_{2g}^- \otimes A_{2g}: \quad \Lambda_1(i\sigma_y)(\cos \kappa_1 - \cos \kappa_2) \sin \kappa_1 \sin \kappa_2,$$

$$E_g^- \otimes E_g: \quad \Lambda_2(\sigma_x \sin \kappa_1 - \sigma_y \sin \kappa_2)(i\sigma_y) \sin \kappa_3,$$

etc. The most general $\Delta(\boldsymbol{k}) \in B_{1g}$ is a linear superposition of all of these.

APPENDIX D: VAN HOVE LINE-GAPPING SC STATES

In Figs. 6–8, we have plotted the Fermi surface projections of a number of Van Hove line gapping even SC states from Table VI. These have been constructed by combining the six A_{1g}^- and B_{1g}^- spin-orbit matrices (Table X) with the lowest order A_{1g}, B_{1g}, and E_g pairing wave functions (Table IX). $\Delta_{\boldsymbol{k}}$ constructed from the highly suppressed E_g^- spin-orbit matrices aren't shown. Of all the possible superpositions in the case of E_g pairing, we have shown the chiral ones as they are the most interesting because of the various evidence [50–56] indicating TRSB. The most general Van Hove line-gapping $\Delta_{\boldsymbol{k}}$ belonging to A_{1g}, B_{1g}, or chiral E_g is a superposition of the shown ones, plus higher order harmonics. $\kappa_1 = ak_1 \in [-\pi, \pi]$, $\kappa_2 = ak_2 \in [-\pi, \pi]$, $\kappa_3 = ck_3 \in [-2\pi, 2\pi]$, and $d_{(x\pm iy)z}(\boldsymbol{k}) = (\sin \frac{\kappa_1}{2} \cos \frac{\kappa_2}{2} \pm i \cos \frac{\kappa_1}{2} \sin \frac{\kappa_2}{2}) \sin \frac{\kappa_3}{2}$. In the γ sheet plots, the Van Hove lines $(\pm\frac{\pi}{a}, 0, k_3)$ and $(0, \pm\frac{\pi}{a}, k_3)$ have been highlighted red. Even though the projections of some $\Delta_{\boldsymbol{k}}$ onto the γ band might be small (shaded blue) near the Van Hove lines [e.g., Fig. 6(b)], they are only exactly zero at a certain κ_3 for the $\Delta_{\boldsymbol{k}} \in E_g$ that have horizontal nodes at $\kappa_3 = 0, \pm 2\pi$.

[1] Y. Maeno, H. Hashimoto, K. Yoshida, S. Nishizaki, T. Fujita, J. G. Bednorz, and F. Lichtenberg, Superconductivity in a layered perovskite without copper, Nature (London) **372**, 532 (1994).

[2] A. P. Mackenzie and Y. Maeno, The superconductivity of Sr₂RuO₄ and the physics of spin-triplet pairing, Rev. Mod. Phys. **75**, 657 (2003).

[3] Y. Maeno, S. Kittaka, T. Nomura, S. Yonezawa, and K. Ishida, Evaluation of spin-triplet superconductivity in Sr₂RuO₄, J. Phys. Soc. Jpn. **81**, 011009 (2012).

[4] C. Kallin, Chiral p-wave order in Sr₂RuO₄, Rep. Prog. Phys. **75**, 042501 (2012).

[5] Y. Liu and Z.-Q. Mao, Unconventional superconductivity in Sr₂RuO₄, Physica C: Superconductivity and its Applications **514**, 339 (2015), Superconducting materials: Conventional, unconventional and undetermined.

[6] A. P. Mackenzie, T. Scaffidi, C. W. Hicks, and Y. Maeno, Even odder after twenty-three years: the superconducting order parameter puzzle of Sr₂RuO₄, npj Quantum Mater. **2**, 40 (2017).

[7] S. A. Kivelson, A. C. Yuan, B. Ramshaw, and R. Thomale, A proposal for reconciling diverse experiments on the superconducting state in Sr₂RuO₄, npj Quantum Mater. **5**, 43 (2020).

[8] A. T. Rømer, A. Kreisel, M. A. Müller, P. J. Hirschfeld, I. M. Eremin, and B. M. Andersen, Theory of strain-induced magnetic order and splitting of T_c and T_{TRSB} in Sr₂RuO₄, Phys. Rev. B **102**, 054506 (2020).

[9] R. Willa, M. Hecker, R. M. Fernandes, and J. Schmalian, Inhomogeneous time-reversal symmetry breaking in Sr₂RuO₄, Phys. Rev. B **104**, 024511 (2021).

[10] A. C. Yuan, E. Berg, and S. A. Kivelson, Strain-induced time reversal breaking and half quantum vortices near a putative superconducting tetracritical point in Sr₂RuO₄, Phys. Rev. B **104**, 054518 (2021).

[11] Y. Sheng, Y. Li, and Y.-f. Yang, Multipole-fluctuation pairing mechanism of $d_{x^2-y^2} + ig$ superconductivity in Sr₂RuO₄, Phys. Rev. B **106**, 054516 (2022).

[12] A. C. Yuan, E. Berg, and S. A. Kivelson, Multiband mean-field theory of the $d + ig$ superconductivity scenario in Sr₂RuO₄, Phys. Rev. B **108**, 014502 (2023).

[13] G. Wagner, H. S. Røising, F. Flicker, and S. H. Simon, Microscopic Ginzburg-Landau theory and singlet ordering in Sr₂RuO₄, Phys. Rev. B **104**, 134506 (2021).

[14] J. Clepkens, A. W. Lindquist, and H.-Y. Kee, Shadowed triplet pairings in Hund's metals with spin-orbit coupling, Phys. Rev. Res. **3**, 013001 (2021).

[15] A. T. Rømer, P. J. Hirschfeld, and B. M. Andersen, Superconducting state of Sr₂RuO₄ in the presence of longer-range Coulomb interactions, Phys. Rev. B **104**, 064507 (2021).

[16] H. G. Suh, H. Menke, P. M. R. Brydon, C. Timm, A. Ramires, and D. F. Agterberg, Stabilizing even-parity chiral superconductivity in Sr₂RuO₄, Phys. Rev. Res. **2**, 032023(R) (2020).

[17] Y. Fukaya, T. Hashimoto, M. Sato, Y. Tanaka, and K. Yada, Spin susceptibility for orbital-singlet cooper pair in the three-dimensional Sr₂RuO₄ superconductor, Phys. Rev. Res. **4**, 013135 (2022).

[18] A. J. Leggett and Y. Liu, Symmetry properties of superconducting order parameter in Sr₂RuO₄, J. Supercond. Novel Magn. **34**, 1647 (2021).

[19] W. Huang, A review of some new perspectives on the theory of superconducting Sr₂RuO₄, Chin. Phys. B **30**, 107403 (2021).

[20] O. Gingras, N. Allaglo, R. Nourafkan, M. Côté, and A. M. S. Tremblay, Superconductivity in correlated multiorbital systems with spin-orbit coupling: Coexistence of even- and odd-frequency pairing, and the case of Sr₂RuO₄, Phys. Rev. B **106**, 064513 (2022).

[21] T. Scaffidi, Degeneracy between even- and odd-parity superconductivity in the quasi-one-dimensional Hubbard model and implications for Sr₂RuO₄, Phys. Rev. B **107**, 014505 (2023).

[22] L. C. Hebel and C. P. Slichter, Nuclear relaxation in superconducting aluminum, Phys. Rev. **107**, 901 (1957); Nuclear spin relaxation in normal and superconducting aluminum, **113**, 1504 (1959).

[23] K. Ishida, Y. Kitaoka, K. Asayama, S. Ikeda, S. Nishizaki, Y. Maeno, K. Yoshida, and T. Fujita, Anisotropic pairing in superconducting Sr₂RuO₄: Ru NMR and NQR studies, Phys. Rev. B **56**, R505 (1997).

[24] K. Ishida, H. Mukuda, Y. Kitaoka, Z. Q. Mao, Y. Mori, and Y. Maeno, Anisotropic Superconducting Gap in the Spin-Triplet

Superconductor Sr_2RuO_4: Evidence From a Ru-NQR Study, Phys. Rev. Lett. **84**, 5387 (2000).

[25] H. Murakawa, K. Ishida, K. Kitagawa, H. Ikeda, Z. Q. Mao, and Y. Maeno, [101]Ru Knight shift measurement of superconducting Sr_2RuO_4 under small magnetic fields parallel to the RuO_2 plane, J. Phys. Soc. Jpn. **76**, 024716 (2007).

[26] A. P. Mackenzie, R. K. W. Haselwimmer, A. W. Tyler, G. G. Lonzarich, Y. Mori, S. Nishizaki, and Y. Maeno, Extremely Strong Dependence of Superconductivity on Disorder in Sr_2RuO_4, Phys. Rev. Lett. **80**, 161 (1998); Erratum: Extremely Strong Dependence of Superconductivity on Disorder in Sr_2RuO_4 [Phys. Rev. Lett. 80, 161 (1998)], **80**, 3890(E) (1998).

[27] Z. Q. Mao, Y. Mori, and Y. Maeno, Suppression of superconductivity in Sr_2RuO_4 caused by defects, Phys. Rev. B **60**, 610 (1999).

[28] N. Kikugawa and Y. Maeno, Non-Fermi-Liquid Behavior in Sr_2RuO_4 with Nonmagnetic Impurities, Phys. Rev. Lett. **89**, 117001 (2002).

[29] N. Kikugawa, A. P. Mackenzie, C. Bergemann, R. A. Borzi, S. A. Grigera, and Y. Maeno, Rigid-band shift of the Fermi level in the strongly correlated metal: $Sr_{2-y}La_yRuO_4$, Phys. Rev. B **70**, 060508(R) (2004).

[30] A. A. Abrikosov and L. P. Gor'kov, Contribution to the theory of superconducting alloys with paramagnetic impurities, ZhETF **39**, 1781 (1960) [Sov. Phys. JETP **12**, 1243 (1961)].

[31] L. P. Gor'kov, Theory of superconducting alloys, in *Superconductivity: Conventional and Unconventional Superconductors*, edited by K. H. Bennemann and J. B. Ketterson (Springer Berlin Heidelberg, Berlin, Heidelberg, 2008), pp. 201–224.

[32] The heating caused by NMR pulses [33,34] has rendered early NMR Knight shift experiments [126], nicely summarized in Fig. 14 of Ref. [25], invalid. The NMR pulse heat-up effect acts on a time scale much shorter than T_1 and has not invalidated the early NMR relaxation rate studies [33]. An early polarized neutron scattering study [127] has been superseded by a new one [36] with better statistics, carried out at a smaller magnetic field.

[33] A. Pustogow, Y. Luo, A. Chronister, Y.-S. Su, D. A. Sokolov, F. Jerzembeck, A. P. Mackenzie, C. W. Hicks, N. Kikugawa, S. Raghu, E. D. Bauer, and S. E. Brown, Constraints on the superconducting order parameter in Sr_2RuO_4 from oxygen-17 nuclear magnetic resonance, Nature (London) **574**, 72 (2019).

[34] K. Ishida, M. Manago, K. Kinjo, and Y. Maeno, Reduction of the [17]O Knight shift in the superconducting state and the heat-up effect by NMR pulses on Sr_2RuO_4, J. Phys. Soc. Jpn. **89**, 034712 (2020).

[35] A. Chronister, A. Pustogow, N. Kikugawa, D. A. Sokolov, F. Jerzembeck, C. W. Hicks, A. P. Mackenzie, E. D. Bauer, and S. E. Brown, Evidence for even parity unconventional superconductivity in Sr_2RuO_4, Proc. Natl. Acad. Sci. USA **118**, e2025313118 (2021).

[36] A. N. Petsch, M. Zhu, M. Enderle, Z. Q. Mao, Y. Maeno, I. I. Mazin, and S. M. Hayden, Reduction of the Spin Susceptibility in the Superconducting State of Sr_2RuO_4 Observed by Polarized Neutron Scattering, Phys. Rev. Lett. **125**, 217004 (2020).

[37] The evidence for a Pauli-limited $B_{c2\|ab}$ is threefold: (i) the SC-normal state transition is first-order below $0.5T_c$, as seen in the hysteresis [47,128,129] and jumps in the specific heat [129,130], thermal conductivity [130], magnetocaloric

effect [128], ac magnetic susceptibility [131], magnetization [47], and Knight shift [35]; (ii) the measured intrinsic SC anisotropy $\xi_{ab}/\xi_c \sim 60$ [46,47] exceeds the critical field anisotropy $B_{c2\|ab}/B_{c2\|c} \sim 20$ [132] by a factor of 3 in the unstrained case, and by a factor of 20 under $\langle 100 \rangle$ uniaxial pressure that maximally enhances T_c [45], whereas for orbitally limited $B_{c2\|ab}$ the two ratios would be comparable; and (iii) $B_{c2\|ab} \propto \Delta/\mu_B \propto T_c$ under small uniaxial strain [103], as expected for Pauli limiting.

[38] A. M. Clogston, Upper Limit for the Critical Field in Hard Superconductors, Phys. Rev. Lett. **9**, 266 (1962).

[39] K. D. Nelson, Z. Q. Mao, Y. Maeno, and Y. Liu, Odd-parity superconductivity in Sr_2RuO_4, Science **306**, 1151 (2004).

[40] J. Jang, D. G. Ferguson, V. Vakaryuk, R. Budakian, S. B. Chung, P. M. Goldbart, and Y. Maeno, Observation of half-height magnetization steps in Sr_2RuO_4, Science **331**, 186 (2011).

[41] Y. Yasui, K. Lahabi, M. S. Anwar, Y. Nakamura, S. Yonezawa, T. Terashima, J. Aarts, and Y. Maeno, Little-Parks oscillations with half-quantum fluxoid features in Sr_2RuO_4 microrings, Phys. Rev. B **96**, 180507(R) (2017).

[42] X. Cai, B. M. Zakrzewski, Y. A. Ying, H.-Y. Kee, M. Sigrist, J. E. Ortmann, W. Sun, Z. Mao, and Y. Liu, Magnetoresistance oscillation study of the spin counterflow half-quantum vortex in doubly connected mesoscopic superconducting cylinders of Sr_2RuO_4, Phys. Rev. B **105**, 224510 (2022).

[43] I. Žutić and I. Mazin, Phase-Sensitive Tests of the Pairing State Symmetry in Sr_2RuO_4, Phys. Rev. Lett. **95**, 217004 (2005).

[44] A. W. Lindquist and H.-Y. Kee, Reconciling the π phase shift in josephson junction experiments with even-parity superconductivity in Sr_2RuO_4, Phys. Rev. B **107**, 014506 (2023).

[45] A. Steppke, L. Zhao, M. E. Barber, T. Scaffidi, F. Jerzembeck, H. Rosner, A. S. Gibbs, Y. Maeno, S. H. Simon, A. P. Mackenzie, and C. W. Hicks, Strong peak in T_c of Sr_2RuO_4 under uniaxial pressure, Science **355**, eaaf9398 (2017).

[46] C. Rastovski, C. D. Dewhurst, W. J. Gannon, D. C. Peets, H. Takatsu, Y. Maeno, M. Ichioka, K. Machida, and M. R. Eskildsen, Anisotropy of the Superconducting State in Sr_2RuO_4, Phys. Rev. Lett. **111**, 087003 (2013).

[47] S. Kittaka, A. Kasahara, T. Sakakibara, D. Shibata, S. Yonezawa, Y. Maeno, K. Tenya, and K. Machida, Sharp magnetization jump at the first-order superconducting transition in Sr_2RuO_4, Phys. Rev. B **90**, 220502(R) (2014).

[48] A. Ramires and M. Sigrist, Identifying detrimental effects for multiorbital superconductivity: Application to Sr_2RuO_4, Phys. Rev. B **94**, 104501 (2016).

[49] A. Ramires and M. Sigrist, A note on the upper critical field of Sr_2RuO_4 under strain, J. Phys.: Conf. Ser. **807**, 052011 (2017).

[50] G. M. Luke, Y. Fudamoto, K. M. Kojima, M. I. Larkin, J. Merrin, B. Nachumi, Y. J. Uemura, Y. Maeno, Z. Q. Mao, Y. Mori, H. Nakamura, and M. Sigrist, Time-reversal symmetry-breaking superconductivity in Sr_2RuO_4, Nature (London) **394**, 558 (1998).

[51] G. Luke, Y. Fudamoto, K. Kojima, M. Larkin, B. Nachumi, Y. Uemura, J. Sonier, Y. Maeno, Z. Mao, Y. Mori, and D. Agterberg, Unconventional superconductivity in Sr_2RuO_4, Phys. B: Condens. Matter **289-290**, 373 (2000).

[52] W. Higemoto, A. Koda, R. Kadono, Y. Yoshida, and Y. Ōnuki, Investigation of spontaneous magnetic field in spin-triplet superconductor Sr_2RuO_4, in *Proceedings of the*

International Symposium on Science Explored by Ultra Slow Muon (USM2013) (2014), https://journals.jps.jp/doi/pdf/10.7566/JPSCP.2.010202.

[53] V. Grinenko, S. Ghosh, R. Sarkar, J.-C. Orain, A. Nikitin, M. Elender, D. Das, Z. Guguchia, F. Brückner, M. E. Barber, J. Park, N. Kikugawa, D. A. Sokolov, J. S. Bobowski, T. Miyoshi, Y. Maeno, A. P. Mackenzie, H. Luetkens, C. W. Hicks, and H.-H. Klauss, Split superconducting and time-reversal symmetry-breaking transitions in Sr_2RuO_4 under stress, Nat. Phys. **17**, 748 (2021).

[54] V. Grinenko, D. Das, R. Gupta, B. Zinkl, N. Kikugawa, Y. Maeno, C. W. Hicks, H.-H. Klauss, M. Sigrist, and R. Khasanov, Unsplit superconducting and time reversal symmetry breaking transitions in Sr_2RuO_4 under hydrostatic pressure and disorder, Nat. Commun. **12**, 3920 (2021).

[55] J. Xia, Y. Maeno, P. T. Beyersdorf, M. M. Fejer, and A. Kapitulnik, High Resolution Polar Kerr Effect Measurements of Sr_2RuO_4: Evidence for Broken Time-Reversal Symmetry in the Superconducting State, Phys. Rev. Lett. **97**, 167002 (2006).

[56] A. Kapitulnik, J. Xia, E. Schemm, and A. Palevski, Polar Kerr effect as probe for time-reversal symmetry breaking in unconventional superconductors, New J. Phys. **11**, 055060 (2009).

[57] K. Saitoh, S. Kashiwaya, H. Kashiwaya, Y. Mawatari, Y. Asano, Y. Tanaka, and Y. Maeno, Inversion symmetry of Josephson current as test of chiral domain wall motion in Sr_2RuO_4, Phys. Rev. B **92**, 100504(R) (2015); Note: contrary to what they say, the inversion symmetry $I_c^+(H) = -I_c^-(-H)$ that becomes restored for small junctions is precisely time-reversal symmetry.

[58] S. Kashiwaya, K. Saitoh, H. Kashiwaya, M. Koyanagi, M. Sato, K. Yada, Y. Tanaka, and Y. Maeno, Time-reversal invariant superconductivity of Sr_2RuO_4 revealed by Josephson effects, Phys. Rev. B **100**, 094530 (2019).

[59] Y.-S. Li, N. Kikugawa, D. A. Sokolov, F. Jerzembeck, A. S. Gibbs, Y. Maeno, C. W. Hicks, J. Schmalian, M. Nicklas, and A. P. Mackenzie, High-sensitivity heat-capacity measurements on Sr_2RuO_4 under uniaxial pressure, Proc. Natl. Acad. Sci. USA **118**, e2020492118 (2021).

[60] Y.-S. Li, M. Garst, J. Schmalian, S. Ghosh, N. Kikugawa, D. A. Sokolov, C. W. Hicks, F. Jerzembeck, M. S. Ikeda, Z. Hu, B. J. Ramshaw, A. W. Rost, M. Nicklas, and A. P. Mackenzie, Elastocaloric determination of the phase diagram of Sr_2RuO_4, Nature (London) **607**, 276 (2022).

[61] V. Grinenko, R. Sarkar, S. Ghosh, D. Das, Z. Guguchia, H. Luetkens, I. Shipulin, A. Ramires, N. Kikugawa, Y. Maeno, K. Ishida, C. W. Hicks, and H.-H. Klauss, μSR measurements on Sr_2RuO_4 under $\langle 110 \rangle$ uniaxial stress, Phys. Rev. B **107**, 024508 (2023).

[62] T. Tamegai, K. Yamazaki, M. Tokunaga, Z. Mao, and Y. Maeno, Search for spontaneous magnetization in Sr_2RuO_4, Physica C: Superconductivity **388-389**, 499 (2003).

[63] P. G. Björnsson, Y. Maeno, M. E. Huber, and K. A. Moler, Scanning magnetic imaging of Sr_2RuO_4, Phys. Rev. B **72**, 012504 (2005).

[64] J. R. Kirtley, C. Kallin, C. W. Hicks, E.-A. Kim, Y. Liu, K. A. Moler, Y. Maeno, and K. D. Nelson, Upper limit on spontaneous supercurrents in Sr_2RuO_4, Phys. Rev. B **76**, 014526 (2007).

[65] C. W. Hicks, J. R. Kirtley, T. M. Lippman, N. C. Koshnick, M. E. Huber, Y. Maeno, W. M. Yuhasz, M. B. Maple, and K. A. Moler, Limits on superconductivity-related magnetization in Sr_2RuO_4 and $PrOs_4Sb_{12}$ from scanning squid microscopy, Phys. Rev. B **81**, 214501 (2010).

[66] P. J. Curran, V. V. Khotkevych, S. J. Bending, A. S. Gibbs, S. L. Lee, and A. P. Mackenzie, Vortex imaging and vortex lattice transitions in superconducting Sr_2RuO_4 single crystals, Phys. Rev. B **84**, 104507 (2011).

[67] P. J. Curran, S. J. Bending, W. M. Desoky, A. S. Gibbs, S. L. Lee, and A. P. Mackenzie, Search for spontaneous edge currents and vortex imaging in Sr_2RuO_4 mesostructures, Phys. Rev. B **89**, 144504 (2014).

[68] E. Mueller, Y. Iguchi, C. Watson, C. Hicks, Y. Maeno, and K. Moler, Constraints on a split superconducting transition under uniaxial strain in Sr_2RuO_4 from scanning squid microscopy, arXiv:2306.13737 [cond-mat.supr-con].

[69] P. J. Curran, S. J. Bending, A. S. Gibbs, and A. P. Mackenzie, The search for spontaneous edge currents in Sr_2RuO_4 mesa structures with controlled geometrical shapes, Sci. Rep. **13**, 12652 (2023).

[70] F. Kidwingira, J. D. Strand, D. J. V. Harlingen, and Y. Maeno, Dynamical superconducting order parameter domains in Sr_2RuO_4, Science **314**, 1267 (2006).

[71] M. S. Anwar, T. Nakamura, S. Yonezawa, M. Yakabe, R. Ishiguro, H. Takayanagi, and Y. Maeno, Anomalous switching in Nb/Ru/Sr_2RuO_4 topological junctions by chiral domain wall motion, Sci. Rep. **3**, 2480 (2013).

[72] M. S. Anwar, R. Ishiguro, T. Nakamura, M. Yakabe, S. Yonezawa, H. Takayanagi, and Y. Maeno, Multicomponent order parameter superconductivity of Sr_2RuO_4 revealed by topological junctions, Phys. Rev. B **95**, 224509 (2017).

[73] C. W. Hicks, D. O. Brodsky, E. A. Yelland, A. S. Gibbs, J. A. N. Bruin, M. E. Barber, S. D. Edkins, K. Nishimura, S. Yonezawa, Y. Maeno, and A. P. Mackenzie, Strong increase of T_c of Sr_2RuO_4 under both tensile and compressive strain, Science **344**, 283 (2014).

[74] M. E. Barber, F. Lechermann, S. V. Streltsov, S. L. Skornyakov, S. Ghosh, B. J. Ramshaw, N. Kikugawa, D. A. Sokolov, A. P. Mackenzie, C. W. Hicks, and I. I. Mazin, Role of correlations in determining the Van Hove strain in Sr_2RuO_4, Phys. Rev. B **100**, 245139 (2019).

[75] C. A. Watson, A. S. Gibbs, A. P. Mackenzie, C. W. Hicks, and K. A. Moler, Micron-scale measurements of low anisotropic strain response of local T_c in Sr_2RuO_4, Phys. Rev. B **98**, 094521 (2018).

[76] H. Matsui, Y. Yoshida, A. Mukai, R. Settai, Y. Ōnuki, H. Takei, N. Kimura, H. Aoki, and N. Toyota, Ultrasonic studies of the spin-triplet order parameter and the collective mode in Sr_2RuO_4, Phys. Rev. B **63**, 060505(R) (2001).

[77] S. Benhabib, C. Lupien, I. Paul, L. Berges, M. Dion, M. Nardone, A. Zitouni, Z. Q. Mao, Y. Maeno, A. Georges, L. Taillefer, and C. Proust, Ultrasound evidence for a two-component superconducting order parameter in Sr_2RuO_4, Nat. Phys. **17**, 194 (2021).

[78] S. Ghosh, A. Shekhter, F. Jerzembeck, N. Kikugawa, D. A. Sokolov, M. Brando, A. P. Mackenzie, C. W. Hicks, and B. J. Ramshaw, Thermodynamic evidence for a two-component superconducting order parameter in Sr_2RuO_4, Nat. Phys. **17**, 199 (2021).

[79] N. Okuda, T. Suzuki, Z. Mao, Y. Maeno, and T. Fujita, Transverse elastic moduli in spin-triplet superconductor Sr_2RuO_4, Physica C: Superconductivity **388-389**, 497 (2003).

[80] F. Jerzembeck *et al.* (unpublished).

[81] S. Ghosh, T. G. Kiely, A. Shekhter, F. Jerzembeck, N. Kikugawa, D. A. Sokolov, A. P. Mackenzie, and B. J. Ramshaw, Strong increase in ultrasound attenuation below T_c in Sr_2RuO_4: Possible evidence for domains, Phys. Rev. B **106**, 024520 (2022).

[82] S. NishiZaki, Y. Maeno, and Z. Mao, Changes in the superconducting state of Sr_2RuO_4 under magnetic fields probed by specific heat, J. Phys. Soc. Jpn. **69**, 572 (2000).

[83] K. Deguchi, Z. Q. Mao, H. Yaguchi, and Y. Maeno, Gap Structure of the Spin-Triplet Superconductor Sr_2RuO_4 Determined from the Field-Orientation Dependence of the Specific Heat, Phys. Rev. Lett. **92**, 047002 (2004).

[84] S. Kittaka, S. Nakamura, T. Sakakibara, N. Kikugawa, T. Terashima, S. Uji, D. A. Sokolov, A. P. Mackenzie, K. Irie, Y. Tsutsumi, K. Suzuki, and K. Machida, Searching for gap zeros in Sr_2RuO_4 via field-angle-dependent specific-heat measurement, J. Phys. Soc. Jpn. **87**, 093703 (2018).

[85] C. Lupien, W. A. MacFarlane, C. Proust, L. Taillefer, Z. Q. Mao, and Y. Maeno, Ultrasound Attenuation in Sr_2RuO_4: An Angle-Resolved Study of the Superconducting Gap Function, Phys. Rev. Lett. **86**, 5986 (2001).

[86] I. Bonalde, B. D. Yanoff, M. B. Salamon, D. J. Van Harlingen, E. M. E. Chia, Z. Q. Mao, and Y. Maeno, Temperature Dependence of the Penetration Depth in Sr_2RuO_4: Evidence for Nodes in the Gap Function, Phys. Rev. Lett. **85**, 4775 (2000).

[87] K. Deguchi, Z. Q. Mao, and Y. Maeno, Determination of the superconducting gap structure in all bands of the spin-triplet superconductor Sr_2RuO_4, J. Phys. Soc. Jpn. **73**, 1313 (2004).

[88] G. E. Volovik, Superconductivity with lines of gap nodes: density of states in the vortex, JETP Lett. **58**, 457 (1993).

[89] M. Suzuki, M. A. Tanatar, N. Kikugawa, Z. Q. Mao, Y. Maeno, and T. Ishiguro, Universal Heat Transport in Sr_2RuO_4, Phys. Rev. Lett. **88**, 227004 (2002).

[90] E. Hassinger, P. Bourgeois-Hope, H. Taniguchi, S. René de Cotret, G. Grissonnanche, M. S. Anwar, Y. Maeno, N. Doiron-Leyraud, and L. Taillefer, Vertical Line Nodes in the Superconducting Gap Structure of Sr_2RuO_4, Phys. Rev. X **7**, 011032 (2017).

[91] P. A. Lee, Localized States in a d-Wave Superconductor, Phys. Rev. Lett. **71**, 1887 (1993).

[92] A. V. Balatsky, M. I. Salkola, and A. Rosengren, Impurity-induced virtual bound states in d-wave superconductors, Phys. Rev. B **51**, 15547 (1995).

[93] Y. Sun and K. Maki, Transport properties of d-wave superconductors with impurities, Europhys. Lett. **32**, 355 (1995).

[94] M. J. Graf, S.-K. Yip, J. A. Sauls, and D. Rainer, Electronic thermal conductivity and the Wiedemann-Franz law for unconventional superconductors, Phys. Rev. B **53**, 15147 (1996).

[95] I. A. Firmo, S. Lederer, C. Lupien, A. P. Mackenzie, J. C. Davis, and S. A. Kivelson, Evidence from tunneling spectroscopy for a quasi-one-dimensional origin of superconductivity in Sr_2RuO_4, Phys. Rev. B **88**, 134521 (2013).

[96] R. Sharma, S. D. Edkins, Z. Wang, A. Kostin, C. Sow, Y. Maeno, A. P. Mackenzie, J. C. S. Davis, and V. Madhavan, Momentum-resolved superconducting energy gaps of Sr_2RuO_4 from quasiparticle interference imaging, Proc. Natl. Acad. Sci. USA **117**, 5222 (2020).

[97] H. Suderow, V. Crespo, I. Guillamon, S. Vieira, F. Servant, P. Lejay, J. P. Brison, and J. Flouquet, A nodeless superconducting gap in Sr_2RuO_4 from tunneling spectroscopy, New J. Phys. **11**, 093004 (2009).

[98] M. A. Tanatar, M. Suzuki, S. Nagai, Z. Q. Mao, Y. Maeno, and T. Ishiguro, Anisotropy of Magnetothermal Conductivity in Sr_2RuO_4, Phys. Rev. Lett. **86**, 2649 (2001).

[99] K. Izawa, H. Takahashi, H. Yamaguchi, Y. Matsuda, M. Suzuki, T. Sasaki, T. Fukase, Y. Yoshida, R. Settai, and Y. Onuki, Superconducting Gap Structure of Spin-Triplet Superconductor Sr_2RuO_4 Studied By Thermal Conductivity, Phys. Rev. Lett. **86**, 2653 (2001).

[100] K. Iida, M. Kofu, K. Suzuki, N. Murai, S. Ohira-Kawamura, R. Kajimoto, Y. Inamura, M. Ishikado, S. Hasegawa, T. Masuda, Y. Yoshida, K. Kakurai, K. Machida, and S. Lee, Horizontal line nodes in Sr_2RuO_4 proved by spin resonance, J. Phys. Soc. Jpn. **89**, 053702 (2020).

[101] K. Jenni, S. Kunkemöller, P. Steffens, Y. Sidis, R. Bewley, Z. Q. Mao, Y. Maeno, and M. Braden, Neutron scattering studies on spin fluctuations in Sr_2RuO_4, Phys. Rev. B **103**, 104511 (2021).

[102] H. Taniguchi, K. Nishimura, S. K. Goh, S. Yonezawa, and Y. Maeno, Higher-T_c superconducting phase in Sr_2RuO_4 induced by in-plane uniaxial pressure, J. Phys. Soc. Jpn. **84**, 014707 (2015).

[103] F. Jerzembeck, A. Steppke, A. Pustogow, Y. Luo, A. Chronister, D. A. Sokolov, N. Kikugawa, Y.-S. Li, M. Nicklas, S. E. Brown, A. P. Mackenzie, and C. W. Hicks, Upper critical field of Sr_2RuO_4 under in-plane uniaxial pressure, Phys. Rev. B **107**, 064509 (2023).

[104] V. Sunko, E. Abarca Morales, I. Marković, M. E. Barber, D. Milosavljević, F. Mazzola, D. A. Sokolov, N. Kikugawa, C. Cacho, P. Dudin, H. Rosner, C. W. Hicks, P. D. C. King, and A. P. Mackenzie, Direct observation of a uniaxial stress-driven Lifshitz transition in Sr_2RuO_4, npj Quantum Mater. **4**, 46 (2019).

[105] R. Balian and N. R. Werthamer, Superconductivity with pairs in a relative p wave, Phys. Rev. **131**, 1553 (1963).

[106] A. Ramires and M. Sigrist, Superconducting order parameter of Sr_2RuO_4: A microscopic perspective, Phys. Rev. B **100**, 104501 (2019).

[107] S.-O. Kaba and D. Sénéchal, Group-theoretical classification of superconducting states of strontium ruthenate, Phys. Rev. B **100**, 214507 (2019); Erratum: Group-theoretical classification of superconducting states of strontium ruthenate [Phys. Rev. B 100, 214507 (2019)], **101**, 209901(E) (2020).

[108] W. Huang, Y. Zhou, and H. Yao, Exotic cooper pairing in multiorbital models of Sr_2RuO_4, Phys. Rev. B **100**, 134506 (2019).

[109] C. Bergemann, A. P. Mackenzie, S. R. Julian, D. Forsythe, and E. Ohmichi, Quasi-two-dimensional Fermi liquid properties of the unconventional superconductor Sr_2RuO_4, Adv. Phys. **52**, 639 (2003).

[110] H. S. Røising, T. Scaffidi, F. Flicker, G. F. Lange, and S. H. Simon, Superconducting order of Sr_2RuO_4 from a three-dimensional microscopic model, Phys. Rev. Res. **1**, 033108 (2019).

[111] A. Tamai, M. Zingl, E. Rozbicki, E. Cappelli, S. Riccò, A. de la Torre, S. McKeown Walker, F. Y. Bruno, P. D. C. King, W. Meevasana, M. Shi, M. Radović, N. C. Plumb, A. S. Gibbs, A. P. Mackenzie, C. Berthod, H. U. R. Strand, M. Kim, A. Georges, and F. Baumberger, High-Resolution Photoemission on Sr$_2$RuO$_4$ Reveals Correlation-Enhanced Effective Spin-Orbit Coupling and Dominantly Local Self-Energies, Phys. Rev. X **9**, 021048 (2019).

[112] M. S. Dresselhaus, G. Dresselhaus, and A. Jorio, *Group Theory: Application to the Physics of Condensed Matter* (Springer Science & Business Media, 2007).

[113] V. Zabolotnyy, D. Evtushinsky, A. Kordyuk, T. Kim, E. Carleschi, B. Doyle, R. Fittipaldi, M. Cuoco, A. Vecchione, and S. Borisenko, Renormalized band structure of Sr$_2$RuO$_4$: A quasiparticle tight-binding approach, J. Electron Spectrosc. Relat. Phenom. **191**, 48 (2013).

[114] S. Cobo, F. Ahn, I. Eremin, and A. Akbari, Anisotropic spin fluctuations in Sr$_2$RuO$_4$: Role of spin-orbit coupling and induced strain, Phys. Rev. B **94**, 224507 (2016).

[115] M. S. Ikeda, J. A. W. Straquadine, A. T. Hristov, T. Worasaran, J. C. Palmstrom, M. Sorensen, P. Walmsley, and I. R. Fisher, Ac elastocaloric effect as a probe for thermodynamic signatures of continuous phase transitions, Rev. Sci. Instrum. **90**, 083902 (2019).

[116] J. A. W. Straquadine, M. S. Ikeda, and I. R. Fisher, Frequency-dependent sensitivity of ac elastocaloric effect measurements explored through analytical and numerical models, Rev. Sci. Instrum. **91**, 083905 (2020).

[117] M. S. Ikeda, T. Worasaran, E. W. Rosenberg, J. C. Palmstrom, S. A. Kivelson, and I. R. Fisher, Elastocaloric signature of nematic fluctuations, Proc. Natl. Acad. Sci. **118**, e2105911118 (2021).

[118] The elastocaloric data of Ref. [60] are available at https://doi.org/10.17630/6a4a06c6-38d3-464f-88d1-df8d2dbf1e75.

[119] See Supplemental Material at http://link.aps.org/supplemental/10.1103/PhysRevB.108.094516 for the data shown in Fig. 2.

[120] J. Sólyom, *Fundamentals of the Physics of Solids, Volume 3 - Normal, Broken-Symmetry, and Correlated Systems* (Springer-Verlag, Berlin, Heidelberg, 2010).

[121] P. Coleman, *Introduction to Many-Body Physics* (Cambridge University Press, 2015).

[122] For the total DOS and gap, we have assumed the form

$$g_{sc}^{tot}(E) = g_{VH} + \Theta(E - \Delta_0)\frac{E}{\sqrt{E^2 - \Delta_0^2}}g_{rest},$$

$$\Delta_0 = 1.76\,k_B T_c \tanh\left(1.76\sqrt{\frac{T_c}{T} - 1}\right),$$

where g_{VH} is the normal-state DOS coming from the parts of the γ sheet that are close to the Van Hove lines and g_{rest} is the remaining normal-state DOS. Both $g_{VH}(\varepsilon_{100}) + g_{rest}(\varepsilon_{100}) \propto S(\varepsilon_{100}, T)/T|_{T>T_c}$ and $T_c(\varepsilon_{100})$ are known experimentally. Only the ratio g_{VH}/g_{rest} needs to be calculated, which we have done using the tight-bind model of Appendix B. One finds that $g_{rest}(\varepsilon_{100})$ is roughly strain-independent, as expected. The entropy is given by Eq. (5).

[123] B. Burganov, C. Adamo, A. Mulder, M. Uchida, P. D. C. King, J. W. Harter, D. E. Shai, A. S. Gibbs, A. P. Mackenzie, R. Uecker, M. Bruetzam, M. R. Beasley, C. J. Fennie, D. G. Schlom, and K. M. Shen, Strain Control of Fermiology and Many-Body Interactions in Two-Dimensional Ruthenates, Phys. Rev. Lett. **116**, 197003 (2016).

[124] C. N. Veenstra, Z.-H. Zhu, M. Raichle, B. M. Ludbrook, A. Nicolaou, B. Slomski, G. Landolt, S. Kittaka, Y. Maeno, J. H. Dil, I. S. Elfimov, M. W. Haverkort, and A. Damascelli, Spin-Orbital Entanglement and the Breakdown of Singlets and Triplets in Sr$_2$RuO$_4$ Revealed By Spin- and Angle-Resolved Photoemission Spectroscopy, Phys. Rev. Lett. **112**, 127002 (2014).

[125] J. Linder and A. V. Balatsky, Odd-frequency superconductivity, Rev. Mod. Phys. **91**, 045005 (2019).

[126] K. Ishida, H. Mukuda, Y. Kitaoka, K. Asayama, Z. Q. Mao, Y. Mori, and Y. Maeno, Spin-triplet superconductivity in Sr$_2$RuO$_4$ identified by ^{17}O Knight shift, Nature (London) **396**, 658 (1998).

[127] J. A. Duffy, S. M. Hayden, Y. Maeno, Z. Mao, J. Kulda, and G. J. McIntyre, Polarized-Neutron Scattering Study of the Cooper-Pair Moment in Sr$_2$RuO$_4$, Phys. Rev. Lett. **85**, 5412 (2000).

[128] S. Yonezawa, T. Kajikawa, and Y. Maeno, First-Order Superconducting Transition Of Sr$_2$RuO$_4$, Phys. Rev. Lett. **110**, 077003 (2013).

[129] S. Yonezawa, T. Kajikawa, and Y. Maeno, Specific-heat evidence of the first-order superconducting transition in Sr$_2$RuO$_4$, J. Phys. Soc. Jpn. **83**, 083706 (2014).

[130] K. Deguchi, M. A. Tanatar, Z. Mao, T. Ishiguro, and Y. Maeno, Superconducting double transition and the upper critical field limit of Sr$_2$RuO$_4$ in parallel magnetic fields, J. Phys. Soc. Jpn. **71**, 2839 (2002).

[131] H. Yaguchi, T. Akima, Z. Mao, Y. Maeno, and T. Ishiguro, Detailed study of the ac susceptibility of Sr$_2$RuO$_4$ in oriented magnetic fields, Phys. Rev. B **66**, 214514 (2002).

[132] S. Kittaka, T. Nakamura, Y. Aono, S. Yonezawa, K. Ishida, and Y. Maeno, Angular dependence of the upper critical field of Sr$_2$RuO$_4$, Phys. Rev. B **80**, 174514 (2009).